SN 2022joj: A Peculiar Type Ia Supernova Possibly Driven by an Asymmetric Helium-shell Double Detonation

Chang Liu (刘畅) [ID],[1,2] Adam A. Miller [ID],[1,2] Ken J. Shen [ID],[3] Samuel J. Boos [ID],[4] Luke Harvey [ID],[5]
Kate Maguire [ID],[5] Steve Schulze [ID],[6] Umut Burgaz [ID],[5] Georgios Dimitriadis [ID],[5] Saarah Hall [ID],[1,2]
Joel Johansson [ID],[7] Charles D. Kilpatrick [ID],[2] Huei Sears [ID],[1,2] Jesper Sollerman [ID],[8] Jacobus H. Terwel [ID],[5,9]
K-Ryan Hinds [ID],[10] Daniel Perley [ID],[10] Matthew J. Graham [ID],[11] Mansi M. Kasliwal [ID],[11] Leander Lacroix [ID],[12,6]
Josiah Purdum [ID],[13] Benjamin Rusholme [ID],[14] and Avery Wold [ID][14]

[1]Department of Physics and Astronomy, Northwestern University, 2145 Sheridan Rd, Evanston, IL 60208, USA
[2]Center for Interdisciplinary Exploration and Research in Astrophysics (CIERA), Northwestern University, 1800 Sherman Ave,
Evanston, IL 60201, USA
[3]Department of Astronomy and Theoretical Astrophysics Center, University of California, Berkeley, CA 94720, USA
[4]Department of Physics & Astronomy, University of Alabama, Tuscaloosa, AL, USA
[5]School of Physics, Trinity College Dublin, The University of Dublin, Dublin 2, Ireland
[6]The Oskar Klein Centre, Department of Physics, Stockholm University, Albanova University Center, SE 106 91 Stockholm, Sweden
[7]Oskar Klein Centre, Department of Physics, Stockholm University, AlbaNova, SE-10691 Stockholm, Sweden
[8]The Oskar Klein Centre, Department of Astronomy, Stockholm University, AlbaNova, SE-106 91 Stockholm, Sweden
[9]Isaac Newton Group (ING), Apt. de correos 321, E-38700, Santa Cruz de La Palma, Canary Islands, Spain
[10]Astrophysics Research Institute, Liverpool John Moores University, Liverpool Science Park, 146 Brownlow Hill, Liverpool L3 5RF, UK
[11]Division of Physics, Mathematics, and Astronomy, California Institute of Technology, Pasadena, CA 91125, USA
[12]LPNHE, CNRS/IN2P3, Sorbonne Université, Université Paris-Cité, Laboratoire de Physique Nucléaire et de Hautes Énergies, 75005
Paris, France
[13]Caltech Optical Observatories, California Institute of Technology, Pasadena, CA 91125, USA
[14]IPAC, California Institute of Technology, 1200 E. California Blvd, Pasadena, CA 91125, USA

ABSTRACT

We present observations of SN 2022joj, a peculiar Type Ia supernova (SN Ia) discovered by the
Zwicky Transient Facility (ZTF). SN 2022joj shows an unusually red $g_{\rm ZTF} - r_{\rm ZTF}$ color at early times
and a rapid blueward evolution afterwards. Around maximum brightness, SN 2022joj shows a high
luminosity ($M_{B,\rm max} = -19.62\,\rm mag$), a blue broadband color ($g_{\rm ZTF} - r_{\rm ZTF} = -0.20\,\rm mag$), and shallow
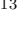Si II absorption lines, consistent with those of overluminous, SN 1991T-like events. Despite the blue
optical-band colors, SN 2022joj exhibits extremely red near-UV colors, suggesting a suppression of
flux between ∼2500–4000 Å. The prominent absorption around 4200 Å, however, resembles the Ti II
features in subluminous, SN 1991bg-like events. We show that these unusual spectroscopic properties
are broadly consistent with the helium-shell double detonation of a sub-Chandrasekhar mass ($M \simeq
1\,\rm M_\odot$) carbon/oxygen (C/O) white dwarf (WD) from a relatively massive helium shell ($M_s \simeq 0.1\,\rm M_\odot$),
if observed along a line of sight roughly opposite to where the shell initially detonates. None of the
existing models could quantitatively explain all the peculiarities observed in SN 2022joj simultaneously.
The low flux ratio of [Ni II] $\lambda 7378$ to [Fe II] $\lambda 7155$ emission in the late-time spectra indicates a low
yields of stable Ni isotopes, favoring a sub-Chandrasekhar mass progenitor. The significant blueshift
measured in the [Fe II] $\lambda 7155$ line is also consistent with an asymmetric chemical distribution in the
ejecta, as is predicted in double detonation models.

1. INTRODUCTION

Type Ia supernovae (SNe Ia) come from thermonuclear
explosions of carbon/oxygen (C/O) white dwarfs (WDs)
in binary systems. While there is broad consensus about
this fact, specifics about the binary companion and the
conditions that spark ignition remain uncertain (e.g.,

Maoz et al. 2014; Liu et al. 2023b, for reviews). Multiple explosion channels have been proposed, though none of them can fully explain the diversity in the SN Ia population.

Recent attention has been focused on the helium-shell double detonation scenario as a potential explanation for some normal SNe Ia (e.g., Polin et al. 2019; Shen et al. 2021b) as well as a growing subclass of peculiar, red SNe Ia (e.g., Jiang et al. 2017; De et al. 2019; Liu et al. 2023a). In a double detonation, the detonation of a helium shell (accreted from a helium-rich companion) atop the primary WD sends a shock wave inward, which eventually converges at some location within the core, triggers a secondary detonation, and inevitably explodes the entire WD (Nomoto 1982a,b; Woosley et al. 1986; Livne 1990; Woosley & Weaver 1994; Livne & Arnett 1995). This mechanism can dynamically ignite WDs well below the Chandrasekhar mass ($M_{\rm Ch}$; $\sim 1.4\,{\rm M_\odot}$). It has been proposed that a substantial fraction of SNe Ia could result from double detonations based on observations of (i) the intrinsic event rate and delay-time distribution (DTD) of the SN Ia population (Ruiter et al. 2011, 2014); (ii) the nucleosynthetic yields of SNe Ia as measured in their late-time spectra (Maguire et al. 2018; Flörs et al. 2020); (iii) the chemical enrichment history of various galaxies (Kirby et al. 2019; de los Reyes et al. 2020; Sanders et al. 2021; Eitner et al. 2022); and (iv) the hyper-velocity Galactic WDs, which are likely surviving donors from double-degenerate binaries where the other WD exploded in a double detonation (Shen et al. 2018b; El-Badry et al. 2023).

The remarkable observational properties for SNe Ia from double detonations are mostly associated with the helium shell. Shortly after the shell detonation, the decay of the radioactive species synthesized during the helium burning may power a flux excess in the early light curves (Woosley & Weaver 1994; Fink et al. 2010; Kromer et al. 2010). Afterwards, the iron-group elements (IGEs) in the helium-shell ashes may provide significant line blanketing bluewards of ~ 5000 Å (Kromer et al. 2010), efficiently suppressing flux in the blue optical. In general, progenitors with a thin helium shell would show minimal detectable effects from the shell detonation, and reproduce "normal" (e.g., that of SN 2011fe; Nugent et al. 2011) luminosity and spectroscopic properties around maximum luminosity (e.g., Polin et al. 2019; Townsley et al. 2019; Magee et al. 2021; Shen et al. 2021b). Normal SNe Ia with a red flux excess shortly after the explosion may be associated with this scenario (e.g., SN 2018aoz; Ni et al. 2022). Meanwhile, objects involving a more massive helium shell exhibit peculiarities, such as a strong flash at early times

and an extremely red color around maximum luminosity (Polin et al. 2019). Several peculiar SNe Ia have been interpreted as double-detonation SNe, including SN 2016jhr (Jiang et al. 2017), SN 2018byg (De et al. 2019), OGLE-2013-SN-079 (Inserra et al. 2015, interpreted as either a pure helium-shell detonation or a double detonation), SN 2016hnk (Jacobson-Galán et al. 2020; but see Galbany et al. 2019 for an alternative interpretation), SN 2016dsg (Dong et al. 2022), SN 2019ofm (De et al. 2020), SN 2020jgb (Liu et al. 2023a), and SN 2019eix (Padilla Gonzalez et al. 2023).

Multidimensional considerations are especially important for double detonations because the initial explosion is triggered far from the center of the WD, and, as a result, all the observables (e.g., luminosities, colors, and absorption line features) are subject to viewing angle effects (Fink et al. 2010; Shen et al. 2021b). Asymmetries in the chemical distribution of the SN Ia ejecta have been invoked to explain SN spectropolarimetric measurements (e.g., Wang et al. 2003; Kasen et al. 2003; Patat et al. 2012, see Wang & Wheeler 2008 for a review) and the kinematics of Ni and Fe in the innermost ejecta (Motohara et al. 2006; Maeda et al. 2010a,b; Maguire et al. 2018; Li et al. 2021). To accurately infer the progenitor of a double-detonation SN, one needs to compare the observations with multidimensional models.

In this paper, we present observations of a peculiar SN Ia, SN 2022joj. SN 2022joj shows a remarkable color evolution, starting with red optical colors that quickly evolve to the blue as the SN rises to maximum luminosity. Its photometric and spectroscopic features are qualitatively consistent with that of a double-detonation SN. In Section 2, we summarize the observations of SN 2022joj, which are analyzed in Section 3, where we show its peculiarities in various aspects. In Section 4.1, we discuss existing scenarios that can lead to a red color in the early light curves of a SN Ia, of which the helium-shell double detonation scenario is the most reasonable explanation. We also show that multidimensional effects have to be accounted for to explain the spectroscopic peculiarities. The indication of a sub-$M_{\rm Ch}$ progenitor and an asymmetric explosion is supported by the late-time spectra of SN 2022joj, which we discuss in Section 4.2. We draw our conclusions in Section 5.

2. OBSERVATIONS

2.1. Discovery & Classification

SN 2022joj was discovered by the Zwicky Transient Facility (ZTF; Bellm et al. 2019a; Graham et al. 2019; Dekany et al. 2020) on 2022 May 08.298 (UT dates are used throughout the paper; MJD 59707.298) with the 48 inch Samuel Oschin Telescope (P48) at Palomar Ob-

servatory, via the ZOGY image differencing algorithm (Zackay et al. 2016), which is utilized by the automated ZTF discovery pipeline (Masci et al. 2019). It was first detected with $r_{ZTF} = 19.13 \pm 0.06$ mag at $\alpha_{J2000} = 14^h41^m40\overset{s}{.}08$, $\delta_{J2000} = +03°00'24''14$ and announced to the public by Fremling (2022). A real-time alert (Patterson et al. 2019) was generated as the candidate passed internal machine-learning thresholds (e.g., Duev et al. 2019; Mahabal et al. 2019), and the internal designation ZTF22aajijjf was assigned. The last 3-σ nondetection limits the brightness to $r_{ZTF} > 21.48$ mag on 2022 May 03.27 (MJD 59702.27; 5.03 days before the first detection) using the ZTF forced photometry from the ZTF Forced Photometry Survice (ZFPS; Masci et al. 2023). SN 2022joj was also independently monitored by the Asteroid Terrestrial-impact Last Alert System (ATLAS; Tonry et al. 2018; Smith et al. 2020). The last 3-σ nondetection with ATLAS was on 2022 May 04.26, 0.99 days after the last nondetection in r_{ZTF}, and with the forced photometry we put a limit of the brightness in the orange filter of $o > 19.84$ mag.

The first spectrum was obtained on 2022 May 11.288 by Newsome et al. (2022), who found a best fit to a young Type I SN at $z = 0.03$ using the Supernova Identification (SNID) algorithm (Blondin & Tonry 2007). In this early spectrum, prominent Si II $\lambda 6355$ and Ca II infrared triplet (IRT) absorption suggest a SN Ia classification, but the overall spectral shape, featuring a relatively red continuum (see Figure 2), is atypical for a normal SN Ia at this phase. Chu et al. (2022) used a maximum luminosity spectrum to indisputably classify SN 2022joj as a SN Ia based on its blue color and persistent Si II features.

2.2. *Host Galaxy*

The host of SN 2022joj is a dwarf galaxy at $\alpha_{J2000} = 14^h41^m40\overset{s}{.}04$, $\delta_{J2000} = +03°00'24''53$, cataloged in the DESI Legacy Imaging Survey (LS; Dey et al. 2019), which reports 3-σ detections in grz and W_1 (see Table 1). SN 2022joj has a projected offset of only $0''5\pm0''1$ to the host (corresponding to a projected distance of 2.7 ± 0.5 kpc at the redshift estimated below).

In addition, the SN field was observed in $grizy$ as part of the wide survey of the Hyper Suprime-Cam Subaru Strategic Program (HSC-SSP; Aihara et al. 2018). We retrieved the stacked science-ready images from the HSC-SSP data archive using the HSC data access tools.[1] The photometry was extracted with the aperture-photometry tool presented by Schulze et al.

(2018). The measurements were calibrated against a set of stars from the Pan-STARRS catalogue, and we applied color terms from the HSC pipeline version 8[2] to correct for differences between the Pan-STARRS and HSC filters. Table 1 summarizes all measurements.

To measure the redshift of the host, we obtained two spectra about 1 year after the maximum brightness of the SN. On 2023 March 14, we took a spectrum of both the SN and the host using Binospec (Fabricant et al. 2019) on the 6.5m MMT telescope with a total integration time of 5400 s. We placed the slit across both the center of the galaxy and the position of the SN (Figure 3). On 2023 April 26, we took another spectrum using the Low Resolution Imaging Spectrometer (LRIS; Oke et al. 1995) on the Keck I 10m telescope. The slit was placed at the same position angle, with the Cassegrain Atmospheric Dispersion Compensator (Cass ADC; Phillips et al. 2006) module on. The total integration time was 3600 s. The LRIS spectrum has a higher signal-to-noise ratio (S/N), in which we detected a potential host emission line at 6742.4 Å (see Figure 3) with a S/N[3] of 3.4. We associated this feature with Hα emission, meaning the corresponding redshift of the host galaxy is $z = 0.02736 \pm 0.0007$, which is in agreement with the initial estimate, $z = 0.03$, from matching the SN spectra to SNID templates (Newsome et al. 2022). In the coadded 2D spectrum, the trace is dominated by the light of the SN in the nebular phase, while the center of this emission feature has an offset of $\sim$3–4 pixels from the center of the trace. The CCDs on LRIS have a pixel scale of $0''135$/pixel, so this offset corresponds to an angular offset of $\sim 0''4$–$0''5$, consistent with the astrometric offset when comparing the LS detection of the host and the ZTF detection of the SN. The Binospec spectrum has a lower S/N, and we cannot identify this emission line at the same position in the 2D spectrum via visual inspection. Nevertheless, we still marginally detect an emission feature in the 1D spectrum with a S/N of 1.5 at the same wavelength. All the evidence indicates that the Hα detection is real.

We estimate the distance modulus of SN 2022joj in the following way. We first use the 2M++ model (Carrick et al. 2015) to estimate the peculiar velocity of the host galaxy to be 244 ± 250 km s^{-1}. Then the peculiar velocity is combined with the recession velocity in the frame of the cosmic microwave background

---

[1] https://hsc-gitlab.mtk.nao.ac.jp/ssp-software/data-access-tools

[2] https://hsc.mtk.nao.ac.jp/pipedoc/pipedoc_8_e/colorterms.html

[3] We fit the emission line with a Gaussian profile to estimate its intensity, and the S/N is defined as the intensity divided by its uncertainty.

Table 1. Host photometry of SN 2022joj.

Survey	Filter	Brightness
		(mag)
HSC-SSP	g	22.01 ± 0.03
HSC-SSP	r	21.63 ± 0.02
HSC-SSP	i	21.54 ± 0.03
HSC-SSP	z	21.37 ± 0.04
HSC-SSP	y	21.22 ± 0.09
LS	g	22.05 ± 0.05
LS	r	21.65 ± 0.05
LS	z	21.39 ± 0.10
LS	W_1	21.94 ± 0.35

NOTE—All magnitudes are reported in the AB system and are not corrected for reddening.

Table 2. Optical and UV Photometry of SN 2022joj.

$t_{\rm obs}$	Flux	$\sigma_{\rm flux}$	Filter	Telescope
(MJD)	(μJy)	(μJy)		
59707.2976	80.8	4.8	$r_{\rm ZTF}$	P48/ZTF
59707.3402	84.9	3.4	$r_{\rm ZTF}$	P48/ZTF
59709.2953	185.5	6.4	$r_{\rm ZTF}$	P48/ZTF
59709.3418	196.5	5.5	$r_{\rm ZTF}$	P48/ZTF
59709.3815	208.0	4.5	$r_{\rm ZTF}$	P48/ZTF

NOTE—Observed fluxes in the ZTF, ATLAS, UVOT, LT, and KAIT passbands, since the first detection in $r_{\rm ZTF}$. Correction for reddening has not been applied.
(This table is available in its entirety in machine readable form.)

(CMB) $v_{\rm CMB} = 8424\,{\rm km\,s^{-1}}$, which yields a net Hubble recession rate of $8193 \pm 250\,{\rm km\,s^{-1}}$. Using cosmological parameters $H_0 = 70\,{\rm km\,s^{-1}\,Mpc^{-1}}$, $\Omega_M = 0.3$, and $\Omega_\Lambda = 0.7$, the estimated luminosity distance to SN 2022joj is 119.5 Mpc, equivalent to a distance modulus of 35.39 ± 0.03 mag.

2.3. *Optical Photometry*

SN 2022joj was monitored in $g_{\rm ZTF}$, $r_{\rm ZTF}$, and $i_{\rm ZTF}$ by ZTF as part of its ongoing Northern Sky Survey (Bellm et al. 2019b). The $i_{\rm ZTF}$ data do not cover the rise. We use the forced-photometry light curves from ZFPS, reduced using the pipeline from A. A. Miller et al. (2023, in preparation); see also Yao et al. (2019). We adopt a Galactic extinction of $E(B-V)_{\rm MW} = 0.032$ mag (Schlafly & Finkbeiner 2011), and correct all photometry using the extinction model from Fitzpatrick (1999) assuming $R_V = 3.1$. We do not find any Na I D absorption at the redshift of the host galaxy (we put a 3-σ upper limit in the equivalent width of Na I $D_1 + D_2$ of <0.5 Å), indicating that the extinction from the host is negligible. The blue $g_{\rm ZTF} - r_{\rm ZTF}$ color (~ -0.2 mag) near maximum luminosity after correcting for the Galactic extinction is also consistent with no additional reddening from the host. Therefore we assume $E(B-V)_{\rm host} = 0$. The dereddened $g_{\rm ZTF}$ and $r_{\rm ZTF}$ forced-photometry light curves in absolute magnitudes are shown in Figure 1. Additional observations of SN 2022joj were obtained in the o and c filters in the ATLAS survey, the $griz$ filters with the optical imaging component of the Infrared-Optical suite of instruments (IO:O) on the Liverpool Telescope, and the gri filters on the Katzmann Automated Imaging Telescope (KAIT). ZTF, ATLAS,

LT, and KAIT observations are reported in Table 2. Given that the LT and KAIT observations were all obtained after maximum light, they are largely excluded from our analysis of the initial evolution of SN 2022joj.

2.4. *Swift Ultraviolet/Optical Telescope (UVOT) Observations*

Ultraviolet (UV) observations of SN 2022joj were obtained using UVOT (Roming et al. 2005) on the Gehrels Swift Observatory (Swift; Gehrels et al. 2004) following a target-of-opportunity (ToO) request by E. Padilla Gonzalez. Prior to the SN, UVOT images of the field had been obtained in the u, $uvw1$, and $uvw2$ filters. In each of these reference images the flux at the location of the SN is consistent with 0, and the 3-σ upper limits correspond to $\lesssim 10\%$ of the SN flux measured in the UV. In the optical bands, the LS photometry ($g = 22.05 \pm 0.05$ mag) shows that the host galaxy contributes $\lesssim 1\%$ of the total observed flux. We therefore conclude that the host galaxy can be neglected when estimating the SN flux in UVOT images.

We estimate the flux in the u, b, v, $uvw1$, $uvm2$, and $uvw2$ filters using a circular aperture with a radius of $5''$ centered at the position of the SN. To estimate the brightness of the sky background we use a coaxial annulus region with an inner/outer radius of $8''/10''$. The reduction is performed with the pipeline `Swift_ToO`[4] based on the package `HEAsoft`[5] version 6.30.1 (HEASARC 2014). The fluxes are also reported in Table 2.

2.5. *Optical Spectroscopy*

---

[4] https://github.com/slowdivePTG/Swift_ToO
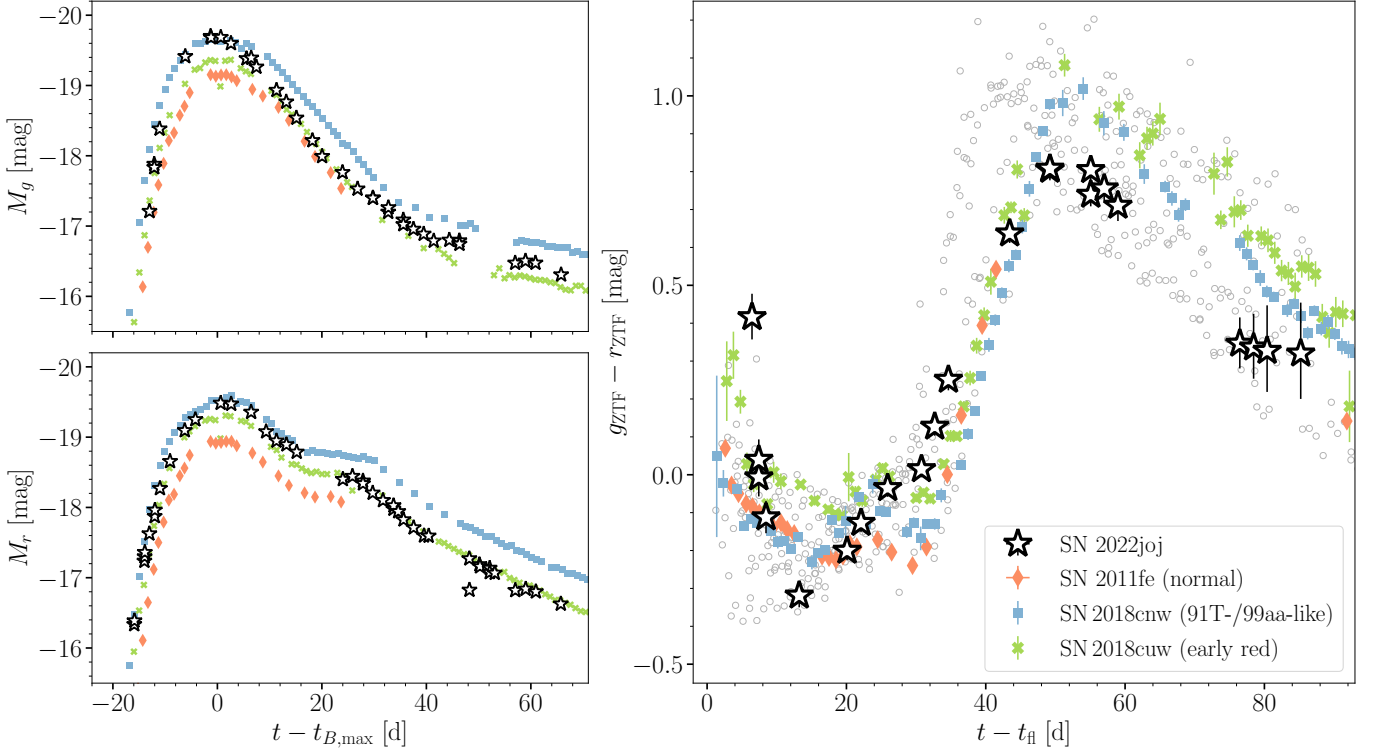[5] http://heasarc.gsfc.nasa.gov/ftools

Figure 1. Comparison of the photometric properties of SN 2022joj with SN 2011fe (normal SN Ia; Pereira et al. 2013), SN 2018cnw (91T-/99aa-like), and SN 2018cuw (normal SN Ia with a red early color). *Left*: multiband light curves. The upper (lower) panel shows the evolution in the g-band (r-band) absolute magnitude. *Right*: $g_{ZTF} - r_{ZTF}$ color evolution. The gray circles denote the color evolution of 14 nearby ($z \leq 0.05$) SNe Ia (open circles) from the ZTF sample with prompt observations within 5 days of first light (Bulla et al. 2020). The phases are measured in the rest frame of the host galaxy. Note that K-corrections have not been applied.

We obtained a series of optical spectra of SN 2022joj using the Spectral Energy Distribution Machine (SEDM; Blagorodnova et al. 2018) on the automated 60 inch telescope (P60; Cenko et al. 2006) at Palomar observatory, the Andalucia Faint Object Spectrograph and Camera (ALFOSC)[6] installed at the 2.56 m Nordic Optical Telescope (NOT), the SPectrograph for the Rapid Acquisition of Transients (SPRAT; Piascik et al. 2014) on the 2 m Liverpool Telescope (LT; Steele et al. 2004) under program PL22A13 (PI: Dimitriadis), the FLOYDS spectrograph[7] on the 2m Faulkes Telescope South (FTS) at Siding Spring as part of the Las Cumbres Observatory (LCO) (Brown et al. 2013), Binospec on the 6.5m MMT telescope, and LRIS on the Keck I 10m telescope. The SEDM spectra were reduced using the custom `pysedm` software package (Rigault et al. 2019). The NOT/ALFOSC, Keck I/LRIS, and MMT/Binospec spectra were reduced using the `PypeIt` package (Prochaska et al. 2020). The LT/SPRAT

spectra were reduced with a dedicated pipeline[8] for bias subtraction, flat fielding, derivation of the wavelength solution and flux calibration, with additional IRAF/PYRAF[9] routines for proper extraction of the spectra. The FTS/FLOYDS spectrum was reduced using the FLOYDS pipeline.[10] Details of the spectroscopic observations are listed in Table 3. The resulting spectral sequence is shown in Figure 2. All the spectra listed in Table 1 will be available on WISeREP (Yaron & Gal-Yam 2012).

We also include the spectrum uploaded to the Transient Name Server (TNS) by Newsome et al. (2022) in our analysis, which is obtained using the FLOYDS spectrograph on the 2m Faulkes Telescope North (FTN) at Haleakala.

---

[6] http://www.not.iac.es/instruments/alfosc/

[7] https://lco.global/observatory/instruments/floyds/

[8] https://github.com/LivTel/sprat_l2_pipeline

[9] IRAF is distributed by the National Optical Astronomy Observatory, which is operated by the Association of Universities for Research in Astronomy (AURA) under a cooperative agreement with the National Science Foundation.

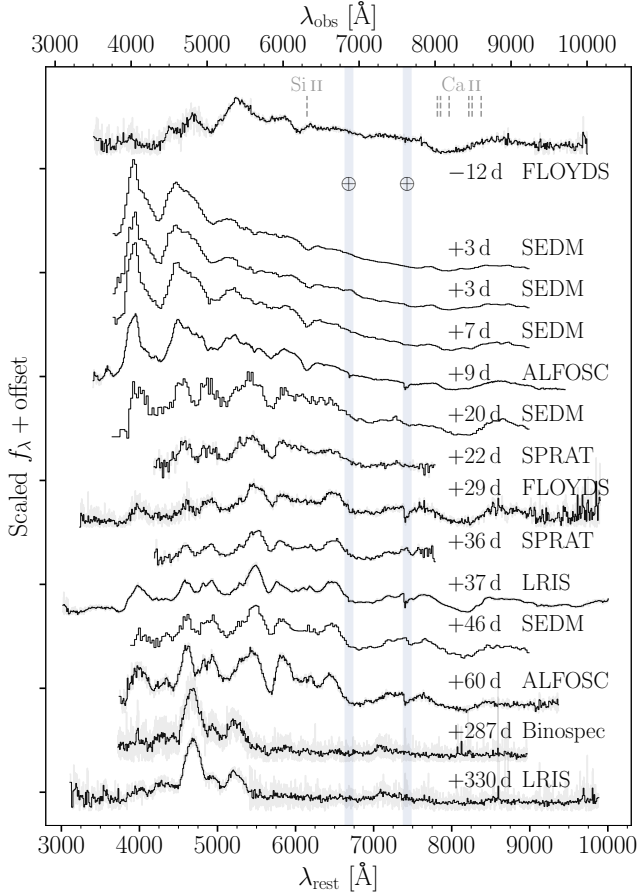[10] https://lco.global/documentation/data/floyds-pipeline/

Figure 2. Optical spectral sequence of SN 2022joj shows the red to blue color transition as the SN rises to its maximum luminosity and the development of prominent absorption features around 4300 Å afterward. Rest-frame phase relative to the B-band peak and the instrument used are listed next to each spectrum. Spectra have been corrected for $E(B-V)_{\rm MW} = 0.032$ mag and are shown in gray. The black lines are binned spectra with a bin size of 10 Å, except for the SEDM spectra, whose resolution is lower than the bin size. The corresponding wavelengths of the Si II $\lambda6355$ line (with an expansion velocity of $10{,}000\,{\rm km\,s^{-1}}$) and the Ca II IRT (with expansion velocities of both $10{,}000\,{\rm km\,s^{-1}}$ and $25{,}000\,{\rm km\,s^{-1}}$) are marked by the vertical dashed lines. The strong optical telluric features (Fraunhofer A and B bands) are marked by the shaded region.

3. ANALYSIS

3.1. *Early Light Curves and the First Light*

To estimate the time of first light ($t_{\rm fl}$), we assume an initial power-law rise in the broad-band flux $f(t)$,

$$f(t) = A(t - t_{\rm fl})^{\alpha},$$

where A is a constant and α is the power-law index. We only include the forced-photometry light curve with flux $\leq 40\%$ of peak luminosity (Miller et al. 2020) in

Table 3. Spectroscopic observations of SN 2022joj.

$t_{\rm obs}$	Phase	Telescope/	R	Range
(MJD)	(days)	Instrument	$(\lambda/\Delta\lambda)$	(Å)
59,710.29	−12.1	FTN/FLOYDS-N	550	3500–10000
59,725.34	+2.5	P60/SEDM	100	3770–9220
59,725.43	+2.6	P60/SEDM	100	3770–9220
59,730.27	+7.3	P60/SEDM	100	3770–9220
59,732.02	+9.0	NOT/ALFOSC	360	3500–9700
59,743.28	+20.0	P60/SEDM	100	3770–9220
59,744.96	+21.6	LT/SPRAT	350	4020–7990
59,752.50	+29.0	FTS/FLOYDS-S	550	3500–10000
59,759.92	+36.2	LT/SPRAT	350	4020–7990
59,760.37	+36.6	Keck I/LRIS	1100	3100–10280
59,770.25	+46.2	P60/SEDM	100	3770–9220
59,784.89	+60.5	NOT/ALFOSC	280	3850–9620
60,017.42	+286.8	MMT/Binospec	1340	3830–9210
60,061.56	+329.8	Keck I/LRIS	1100	3200–10150

Note—Phase is measured relative to the B-band peak in the rest frame of the host galaxy. The resolution R is reported for the central region of the spectrum.

$r_{\rm ZTF}$ and ATLAS o, in which observations were conducted on more than three nights between -20 days and -10 days. Light curves in other bands are excluded because the coverage is significantly worse at this phase (see Section 3.2). We assume that the $t_{\rm fl}$ is the same in both bands, then estimate α and A in each band with a Bayesian approach. We adopt flat priors for $t_{\rm fl}$ and $\log A$, and a normal prior for each α centered at 2 (the fireball model) with a standard deviation of 1. We sample their posterior distributions with Markov Chain Monte Carlo (MCMC) using the package `PyMC` (Salvatier et al. 2016). In addition, we run another model with a fixed $\alpha = 2$. The estimated model parameters are listed in Table 4. We find that both light curves are consistent with a power-law rise since MJD $59703.16^{+0.70}_{-0.58}$, and there is no evidence for significantly different $t_{\rm fl}$ in two bands. This estimate is consistent with the $\alpha = 2$ fireball model. When fixing $\alpha = 2$, the model also fits the light curve well, but the estimated $t_{\rm fl}$ is ~ 0.5 day later (MJD $59703.66^{+0.10}_{-0.11}$). We do not find any correlated residuals as evidence for a flux excess after ~ 4 days since $t_{\rm fl}$, although a flux excess before the first detection could not be ruled out.

3.2. *Photometric Properties*

The basic photometric properties of SN 2022joj are listed in Table 4. The times of the maximum luminosity and the corresponding magnitudes in the ZTF g and r bands are estimated using a fourth-order polynomial fit. We do not include the maximum $i_{\rm ZTF}$-band properties, which are relatively uncertain due to the low
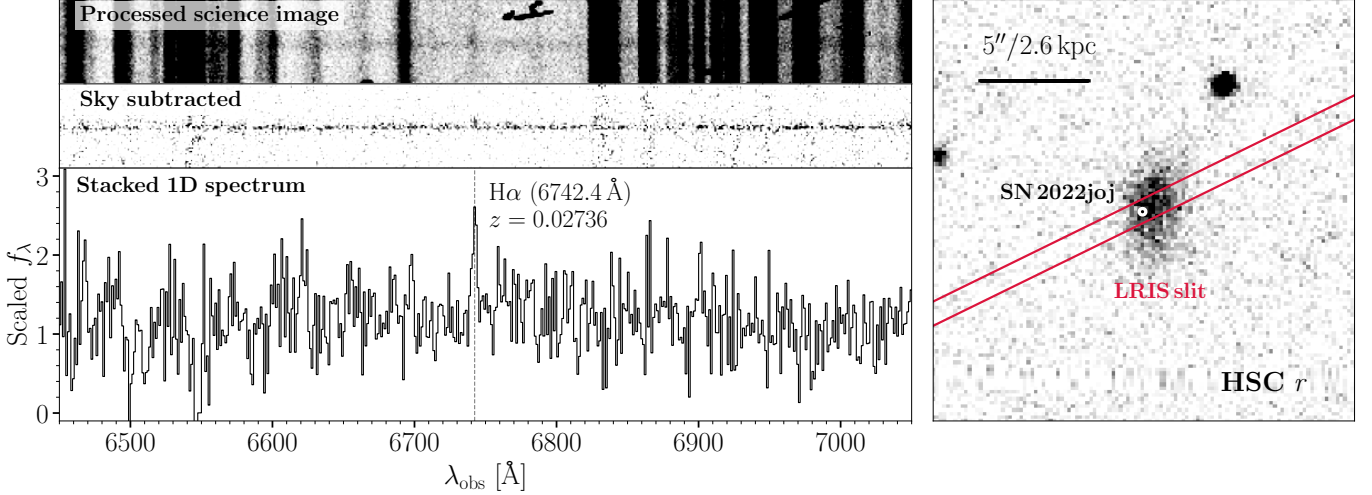
Figure 3. The LRIS spectrum reveals an Hα emission line from the host galaxy at 6742.4 Å, corresponding to a redshift $z = 0.02736$. *Left:* the Hα emission in the observed 2D and 1D spectrum. This emission line sits in the region free of strong sky lines and is unlikely due to bad sky subtraction. *Right:* image of the host galaxy and the position of SN 2022joj, with the orientation of the LRIS slit overplotted.

cadance in i_{ZTF} around peak. In addition, we feed the UVOT b and v, ZTF g, r, and i, as well as ATLAS c and o light curves simultaneously to the `SALT3` (Kenworthy et al. 2021) model with the package `sncosmo` (Barbary et al. 2023), which enable us to estimate the Bessell B-band properties. However, we find that the `SALT3` model cannot reproduce the broadband colors at maximum luminosity. It underestimates the maximum brightness in g_{ZTF} and r_{ZTF}. The predicted M_{max} in g_{ZTF} (r_{ZTF}) is 0.04 mag (0.07 mag) fainter than the highest observed flux. Meanwhile, it overestimates the maximum brightness in UVOT b by 0.16 mag. This indicates that SN 2022joj is a peculiar event compared with the SNe Ia included in SALT3 light curve templates, and we thus do not use the t_{max} and M_{max} provided in the `SALT3` fit. Instead, we adopt the epoch (MJD 59722.75) and the magnitude (-19.62 ± 0.03 mag; corrected for Galactic extinction) of the last Swift observation in UVOT b as the t_{max} and M_{max} in Bessell B.[11]

SN 2022joj shows a few peculiar photometric features compared to normal SNe Ia. In Figure 1, we compare the g_{ZTF} and r_{ZTF} light curves and the $g_{\mathrm{ZTF}} - r_{\mathrm{ZTF}}$ color evolution of SN 2022joj with those of the well-observed normal SN Ia, SN 2011fe,[12] as well as SN 2018cnw (ZTF18abauprj) and SN 2018cuw (ZTF18abcflnz) from a sample of SNe Ia with prompt observations within

5 days of first light by ZTF (Yao et al. 2019; Bulla et al. 2020). SN 2018cnw is slightly overluminous at peak, and belongs to either the SN 1999aa-like (99aa-like; Garavini et al. 2004) or SN 1991T-like (91T-like; Filippenko et al. 1992a) subclass of SNe Ia, while SN 2018cuw is a normal SN Ia with a red $g_{\mathrm{ZTF}} - r_{\mathrm{ZTF}}$ color comparable to that of SN 2022joj ~15 days prior to peak.

Around maximum brightness, SN 2022joj is overluminous, comparable to SN 2018cnw, and ~0.5 mag brighter than SN 2011fe in both g_{ZTF} and r_{ZTF}. But SN 2022joj clearly stands out due to its fast evolution in g_{ZTF}. While SN 2022joj and SN 2018cnw show a similar maximum brightness in g_{ZTF}, upon the first detection of SN 2022joj in g_{ZTF} at ~-13 days, its corresponding absolute magnitude (-17.2 mag) is ~0.8 mag fainter than that of SN 2018cnw at a similar phase. This means on average, SN 2022joj rises faster than SN 2018cnw by ~0.06 mag day^{-1} in g_{ZTF} during that period of time. On the decline, the $\Delta m_{15}(g_{\mathrm{ZTF}})$ of SN 2022joj is 1.03 ± 0.03 mag, which is significantly greater than that of the overluminous SN 2018cnw ($\Delta m_{15}(g_{\mathrm{ZTF}}) = 0.77$ mag) or normal SN 2011fe ($\Delta m_{15}(g_{\mathrm{ZTF}}) = 0.80$ mag). The rapid decline of SN 2022joj is atypical for overluminous SNe Ia, which are usually the slowest decliners in the SN Ia population (Phillips et al. 1999; Taubenberger 2017). The rapid decline is probably due to the unusual and fast-developing absorption feature near 4200 Å (see Section 3.3).

The color evolution of SN 2022joj does not match that of normal SNe Ia, as shown by the trail traced by SN 2022joj in the right panel of Figure 1. We overplot all the SNe from the ZTF early SN Ia sam-

[11] There are known color terms in the transformation between UVOT b and Bessell B (Poole et al. 2008). When $b - v \simeq 0$ mag, as is observed in SN 2022joj around maximum brightness, $B - b \lesssim 0.02$ mag.

[12] We show the synthetic photometry in g_{ZTF} and r_{ZTF} calculated using the spectrophotometric sequence from Pereira et al. (2013).

ple (Bulla et al. 2020) with a redshift $z \leq 0.05$. They are corrected for Galactic extinction, but K-corrections have not been performed for consistency. Given the peculiar nature of SN 2022joj, we cannot use models trained on normal SNe Ia to reliably estimate its K-correction. Nevertheless, given its relatively low redshift ($z \lesssim 0.03$), the K-corrections are not expected to be large ($K(g_{\rm ZTF} - r_{\rm ZTF}) \simeq -0.07\,\rm mag$ around maximum, estimated using the SEDM spectrum at $+2.5\,\rm days$). For the same reason we only include the SNe Ia with the lowest redshift from the sample of Bulla et al. (2020). SN 2022joj is remarkably red ($g_{\rm ZTF} - r_{\rm ZTF} \simeq 0.4\,\rm mag$) around ∼7 days after $t_{\rm fl}$, and is clearly an outlier compared to the normal SN Ia sample.[13] During the ensuing week, SN 2022joj quickly evolves to the blue, and is among the bluest objects in the sample ∼15 days after $t_{\rm fl}$ ($g_{\rm ZTF} - r_{\rm ZTF} \simeq -0.5\,\rm mag$). SN 2018cuw has a comparable $g_{\rm ZTF} - r_{\rm ZTF}$ color at early times, but the blueward evolution of SN 2018cuw is slower than that of SN 2022joj. From ∼10–20 days after $t_{\rm fl}$, SN 2022joj starts to evolve redward. While other SNe Ia show qualitatively similar redward evolution, this usually happens at a much later phase (∼30 days after $t_{\rm fl}$). When $g_{\rm ZTF} - r_{\rm ZTF}$ reaches maximum (∼0.8 mag) ∼50 days after $t_{\rm fl}$, SN 2022joj is again bluer than most of the SNe Ia in the ZTF sample. Eventually as SN 2022joj steps into the transitional phase, its color evolution follows the Lira law[14] (Lira 1996; Phillips et al. 1999) and shows no significant difference from that of the SNe Ia in the ZTF sample.

While SN 2022joj shows a blue $g_{\rm ZTF} - r_{\rm ZTF}$ color near maximum, its near-UV colors are unusually red. In Figure 4, we show the locations of SN 2022joj in the UVOT color-color diagrams compared to that of 29 normal SNe Ia with UV observations around maximum from Brown et al. (2018). SN 2022joj stands out due to the red $u-v$ and $uvw1-v$ colors. After correcting for Galactic extinction, SN 2022joj shows $u - v = 1.59^{+0.06}_{-0.06}\,\rm mag$ and $uvw1 - v = 3.99^{+0.23}_{-0.19}\,\rm mag$. As a comparison, none of the objects in the normal SN Ia sample shows $u-v > 0.5\,\rm mag$ or $uvw1-v > 2.1\,\rm mag$. This cannot be a result of the unknown host reddening, since the amount of host extinction needed to account for the red near-UV colors of SN 2022joj would require the intrinsic $b-v$ color of the SN to be unphysically blue (Figure 4). In-

terestingly, SN 2022joj shows a moderately blue mid-UV color ($uvm2 - uvw1 = 1.52^{+0.48}_{-0.33}\,\rm mag$), while most of the normal SNe Ia in the sample from Brown et al. (2018) show $uvm2 - uvw1 \gtrsim 2\,\rm mag$. This might indicate that, for some reason, the flux in near-UV (∼2500–4000 Å) of SN 2022joj is suppressed near maximum brightness.

To conclude, despite a similar luminosity and color to 99aa-like/91T-like events at maximum brightness, the rapid photometric rise and decline and the unusual color evolution in SN 2022joj both indicate that it exhibits some peculiarities relative to normal and 99aa-like/91T-like SNe Ia.

3.3. *Optical Spectral Properties*

In Figure 2, we show the optical spectral sequence of SN 2022joj. The −12 days spectrum exhibits prominent absorption lines associated with Si II λ6355 and Ca II IRT (this spectrum was obtained and posted on TNS by Newsome et al. 2022). It also shows a strong suppression of flux blueward of ∼5000 Å, confirming the unusually red photometric colors at early times. Near maximum brightness, the two SEDM spectra show a very blue continuum between ∼5000–8000 Å with shallow absorption features, indicating a high photometric temperature. Si II $\lambda\lambda$5972, 6355 lines, the S II W-trough, and Ca II IRT are detectable but not prominent. A wide, asymmetric absorption feature appears between ∼4000–4500 Å (the 4200 Å features hereafter). There is a break on the blue edge of this feature which could be associated with Si II λ4128 that is often seen in other SNe Ia. However, the spectra of most normal and overluminous 99aa-like/91T-like SNe Ia show another peak at ∼4100–4200 Å redward of a narrow Si II λ4128 feature, which is absent in the spectra of SN 2022joj (see the left panel of Figure 5). The 4200 Å features become even wider and deeper in another SEDM spectrum at +7 days and the ALFOSC spectrum at +9 days. Weeks after the maximum, in the FLOYDS spectrum (+29 days) and the LRIS spectrum (+36 days), the bottom of the 4200 Å features becomes flat, reminiscent of the Ti-trough in the subluminous SN 1991bg-like (91bg-like; Filippenko et al. 1992b; Leibundgut et al. 1993) SNe. The nebular-phase spectra are dominated by [Fe II], [Fe III], and [Co III] emission lines, but the [Fe II] features (e.g, the complex around ∼7300 Å) are weaker than in other SNe Ia, suggesting that the ejecta remain highly ionized. The nebular spectra are discussed in detail in Section 4.2.

In Figure 5, we compare maximum light and transition phase spectra of SN 2022joj to those seen in other SNe Ia. Around peak, the blue continuum and shallow absorp-

---

[13] There is one point close to the first detection of SN 2022joj in the color evolution diagram, which belongs to SN 2018dhw (ZTF18abfhryc). This single $g_{\rm ZTF} - r_{\rm ZTF}$ measurement has an uncertainty of ∼0.1 mag and is 2-σ redder than measurements made the night before and after.

[14] The original Lira law was discovered in the $B - V$ color, but in the $g_{\rm ZTF} - r_{\rm ZTF}$ color we see a similar trend.
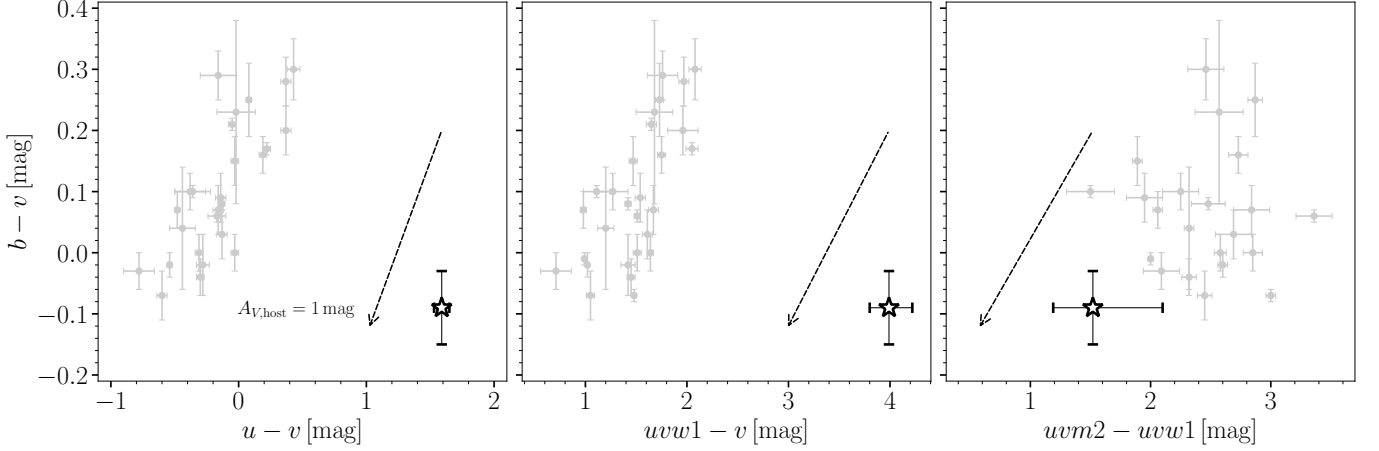
Figure 4. The color-color diagrams using UVOT photometry show that SN 2022joj (black star) has very unusual UV colors at maximum luminosity compared to normal SNe Ia (gray dots; a sample of 29 normal SNe Ia from Brown et al. 2018). The dashed arrows mark how SN 2022joj would move in each color-color space if there were non-negligible host reddening with the visual extinction up to $A_{V,\mathrm{host}} = 1$ (assuming $R_V = 3.1$).

Table 4. Basic photometric properties of SN 2022joj.

Rise (flux $\leq$40% of peak luminosity)			
t_{fl} (MJD)	$59703.16^{+0.70}_{-0.58}$		
$\alpha_{\mathrm{ZTF},r}$	$2.18^{+0.20}_{-0.24}$		
$\alpha_{\mathrm{ATLAS},o}$	$2.37^{+0.48}_{-0.20}$		
$t_{\mathrm{fl},\alpha=2}$ (MJD)	$59703.66^{+0.10}_{-0.11}$		
Maximum luminosity			
Filters	g_{ZTF}	r_{ZTF}	B
$t_{\mathrm{max,poly}}$ (MJD)	59722.65 ± 0.22	59725.13 ± 0.08	$\cdots$
$M_{\mathrm{max,poly}}$ (mag)	-19.693 ± 0.013	-19.489 ± 0.004	$\cdots$
$t_{\mathrm{max,SALT}}$ (MJD)	59724.16 ± 0.04	59725.26 ± 0.03	59723.36 ± 0.04
$M_{\mathrm{max,SALT}}$ (mag)	-19.663 ± 0.007	-19.409 ± 0.002	-19.780 ± 0.009

NOTE—The absolute magnitudes have been corrected for Galactic extinction. The uncertainty in the distance modulus (0.03 mag) and the systematics in the SALT3 models are not included.

tion features in SN 2022joj are similar to that of overluminous objects, including SN 1991T, SN 1999aa, and SN 2000cx. The asymmetric 4200 Å features are not seen in SN 1991T or SN 1999aa, while in SN 2000cx, a similar (but narrower) absorption feature is interpreted as high velocity Ti II (Branch et al. 2004). The 4200 Å features are actually much more similar to the well-known Ti-trough that is ubiquitous in subluminous 91bg-like objects, e.g., SN 1999by (Arbour et al. 1999). Prior to the peak, SN 1999by also shows this asymmetric absorption at about the same wavelength. In 91bg-like SNe, this absorption feature becomes more prominent with a nearly flat-bottom trough about a week after maximum. This absorption is caused by a blend of multiple species dominated by Ti II (Filippenko et al. 1992b; Mazzali et al. 1997). It remains prominent in

the spectrum up to one month after maximum. Similarly, we find that this trough is prominent in the spectra of SN 2022joj at +29 days and +36 days. Other normal/overluminous SNe Ia, unlike SN 2022joj, all exhibit a dip around ∼4500 Å. Aside from the 4200 Å features, SN 2022joj is otherwise entirely dissimilar to 91bg-like objects, which are $\gtrsim$2 mag fainter at peak and exhibit much stronger Si II, Ca II and O I absorption from a cooler line-forming region (Filippenko et al. 1992b). The Ti-trough in 91bg-like SNe is interpreted as the result of a low photospheric temperature (Mazzali et al. 1997). Whether the 4200 Å features in SN 2022joj are dominated by Ti II absorption is unclear.

SN 2022joj also shows remarkably shallow Si II absorption at maximum brightness. Following the techniques elaborated in Liu et al. (2023a) (see also Childress et al.
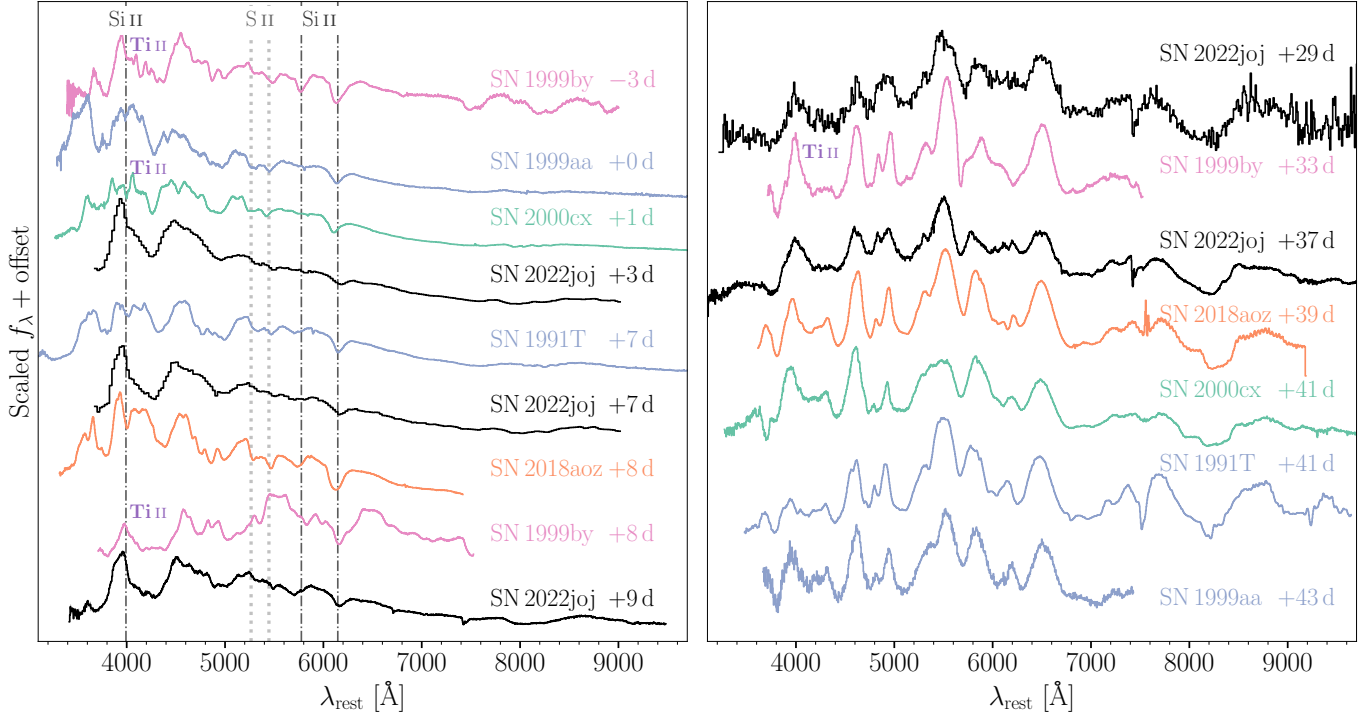
Figure 5. Optical spectra of SN 2022joj (black) and (i) a subluminous SN Ia, SN 1999by (magenta), (ii) two overluminous SNe Ia, SN 1991T and SN 1999aa (blue), (iii) the peculiar SN 2000cx (green), and (iv) a normal SN Ia with a red color at early times, SN 2018aoz (orange), near maximum brightness (left panel) and a month after maximum (right panel). The dash-dotted lines correspond to wavelengths of three Si II lines (4128 Å, 5972 Å, and 6355 Å), while the dotted lines correspond to the wavelengths of the S II W-trough (both assuming an expansion velocity of $10,000 \, \mathrm{km \, s^{-1}}$). Ti II has been identified from the spectra of SN 1999by and SN 2000cx at around ~4200 Å, and the corresponding features are labeled. Spectra were downloaded from WiseREP (Yaron & Gal-Yam 2012), with the following original data sources: SN 1991T, SN 1999aa, and SN 2000cx – Silverman et al. (2012); SN 1999by – Matheson et al. (2008); SN 2018aoz – Ni et al. (2023).

2013, 2014; Maguire et al. 2014), we fit the Si II and Ca II IRT features with multiple Gaussian profiles. We find that modeling the Ca II IRT absorption requires two distinct velocity components – the photospheric velocity features (PVFs) and the high velocity features (HVFs). In Table 5 we list the estimates of the expansion velocities and the pseudo-equivalent widths (pEWs) of the major absorption lines from −12 days to +9 days. In Figure 6 we show the peak absolute magnitude in B band vs. the velocity and pEW of Si II for SN 2022joj and a sample of normal SNe Ia from Zheng et al. (2018) and Burrow et al. (2020). Figure 6 highlights that SN 2022joj is slightly overluminous with a relatively low Si II λ6355 expansion velocity (hereafter $v_{\mathrm{Si \, II}}$). The Si II λ5972 and Si II λ6355 pEWs in SN 2022joj are lower than that for most normal SNe Ia. In fact, SN 2022joj sits at the extreme edge of the shallow-silicon group proposed in Branch et al. (2006), which mainly consists of overluminous 91T-like/99aa-like objects. This is consistent with the high luminosity and the blue color of SN 2022joj at maximum light, since a high photometric temperature results in higher ionization, reducing the abundance

of singly ionized atoms (e.g., Si II). Interestingly, the pEW of Si II λ6355 near peak is significantly lower than that in the first spectrum. In typical 91T-like/99aa-like objects, the Si II features are weak or undetectable at early times because the ejecta are even hotter, and only start to emerge around maximum light (Filippenko et al. 1992a). In the early spectrum of SN 2022joj, in contrast, stronger absorption features from singly ionized Si and Ca indicate a cooler line-forming region at early times compared to that at maximum brightness.

In conclusion, the spectral evolution of SN 2022joj shows some similarities to 91T-like/99aa-like objects, as well as peculiarities. A reasonable model to explain SN 2022joj needs to reproduce (i) a strong suppression in flux blueward of ~5000 Å at early times followed by a rapid evolution to blue colors; (ii) the seemingly contradictory observables at peak, namely the tentative Ti II features and the blue continuum/shallow Si II feature at maximum, which separately indicate low and high photometric temperatures, respectively.
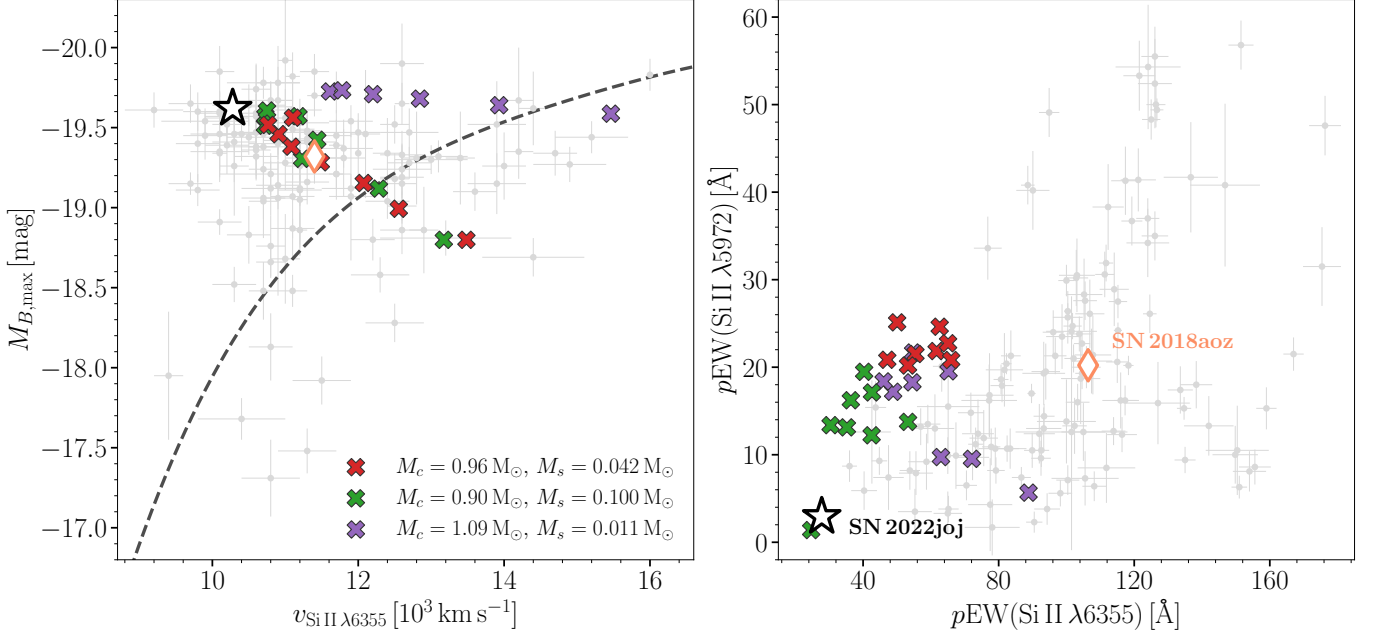
Figure 6. SN 2022joj (black star) as an overluminous SN Ia marked by its shallow Si II features. *Left:* the B-band absolute magnitude versus the expansion velocity of Si II $\lambda6355$ at maximum brightness. *Right:* the pseudo-equivalent width (pEW) of the two Si II lines, Si II $\lambda\lambda5972, 6355$, at maximum brightness. The grey dots show normal SNe Ia from Zheng et al. (2018) and Burrow et al. (2020). The dashed black line corresponds to the theoretical $M_{B,\mathrm{max}}$-$v_{\mathrm{Si\,II}}$ relation of 1D double detonation models for thin helium shells across a spectrum of progenitor masses in Polin et al. (2019). The colored × symbols show 2D double detonation models from Shen et al. (2021b) with different C/O core mass (M_c) and helium shell mass (M_s), and viewing angles (μ defined as the cosine of the polar angle relative to the point where the helium-shell detonation occurs). For each model, multiple symbols are shown to summarize the effect of different viewing angles, from $\mu = -0.93$ to $\mu = +0.93$. Parameters of the potential double-detonation normal SN Ia, SN 2018aoz (Ni et al. 2023), are also overplotted as an orange diamond.

Table 5. Fits to the expansion velocities and pEWs of Si II $\lambda\lambda5972, 6355$ and the Ca II IRT of SN 2022joj.

	Si II $\lambda5972$		Si II $\lambda6355$		Ca II IRT, PVFs		Ca II IRT, HVFs	
Phase	v	pEW	v	pEW	v	pEW	v	pEW
(day)	($10^3\,\mathrm{km\,s^{-1}}$)	(Å)	($10^3\,\mathrm{km\,s^{-1}}$)	(Å)	($10^3\,\mathrm{km\,s^{-1}}$)	(Å)	($10^3\,\mathrm{km\,s^{-1}}$)	(Å)
-12.1	$\cdots$	$\cdots$	-15.66 ± 0.13	47.5 ± 2.5	-14.85 ± 0.83	190 ± 34	-25.98 ± 0.56	278 ± 40
$+2.5$	-8.77 ± 0.63	2.9 ± 1.5	-10.28 ± 0.13	27.8 ± 1.3	-12.03 ± 0.73	58 ± 11	-22.51 ± 0.33	109 ± 11
$+2.6$	-8.35 ± 0.62	4.4 ± 2.6	-9.87 ± 0.28	25.4 ± 2.7	-11.77 ± 0.93	85 ± 17	-22.17 ± 0.47	105 ± 15
$+7.3$	$\cdots$	$\cdots$	-10.52 ± 0.17	40.9 ± 2.7	-10.10 ± 0.82	79 ± 18	-20.88 ± 0.57	172 ± 24
$+9.0$	$\cdots$	$\cdots$	-10.37 ± 0.04	48.5 ± 0.6	-11.94 ± 0.23	144 ± 6	-21.13 ± 0.15	127 ± 6

3.4. *Host Galaxy Properties*

We model the observed spectral energy distribution (SED; photometry in HSC-SSP *grizy* and LS W_1 fil-

ters) with the software package `Prospector`[15] version 1.1 (Johnson et al. 2021a). The LS *grz* photometry,

---

[15] `Prospector` uses the `Flexible Stellar Population Synthesis` (`FSPS`) code (Conroy et al. 2009a) to generate the underlying physical model and `python-fsps` (Foreman-Mackey et al. 2014) to interface with `FSPS` in `python`. The `FSPS` code also accounts for the contribution from the diffuse gas based on the `Cloudy` models from Byler et al. (2017). We use the dynamic nested sampling package `dynesty` (Speagle 2020a) to sample the posterior probability.

which is consistent with the HSC-SSP results but shows a lower S/N, is excluded from this modeling. We assume a Chabrier IMF (Chabrier 2003) and approximate the star formation history (SFH) by a linearly increasing SFH at early times followed by an exponential decline at late times (functional form $t \times \exp{(-t/\tau)}$, where t is the age of the SFH episode and τ is the e-folding timescale). The model is attenuated with the Calzetti et al. (2000) model. The priors of the model parameters are set identically to those used by Schulze et al. (2021).

The SED is adequately described by a galaxy template with a mass of $\log(M_*/\mathrm{M}_\odot) = 7.13^{+0.15}_{-0.28}$, suggesting that the host is a dwarf galaxy. The modeled star formation rate (SFR) is consistent with 0, but we note that measuring low SFRs with SED fitting is not robust, which is subject to systematics (Conroy 2013). In addition, the Hα emission detected in the late-time spectrum of the SN (Section 2.2) indicates at least some level of star formation in the host.

4. DISCUSSION

4.1. SN 2022joj Compared to Model Explosions

There are several physical mechanisms that can produce blue colors during the early evolution of SNe Ia, including: heating of the SN ejecta following the decay of radioactive ^{56}Ni, interaction of the SN ejecta with a nondegenerate companion (e.g., Kasen 2010), collisions between the SN ejecta and circumstellar material (e.g., Piro & Morozova 2016), strong mixing that surfaces ^{56}Ni to the outermost layers of the ejecta (e.g., Piro & Nakar 2013; Magee & Maguire 2020), and/or the production of radioactive isotopes in the detonation of a helium shell on the surface of the exploding WD (e.g., Noebauer et al. 2017; Polin et al. 2019).

On the other hand, there are few proposed scenarios that can produce red colors up to a week after explosion, as is the case of SN 2022joj. If the newly synthesized ^{56}Ni is strongly confined to the innermost SN ejecta, then a SN may remain red for several days after explosion as the heating diffuses out towards the photosphere (Piro & Morozova 2016). Even the most confined ^{56}Ni configuration considered in Piro & Morozova (2016) converges to blue colors, similar to explosions with more extended ^{56}Ni distributions, within ∼6 days after explosion. SN 2022joj is observed to have very red colors ∼7 days after t_fl (meaning more than 7 days after explosion, since SNe Ia have a "dark phase" before photons diffuse out of the ejecta; Piro & Nakar 2013). Dessart et al. (2014) considered more realistic delayed-detonation scenarios. Some of their 1D unmixed delayed-detonation models still show a red $B-R$ color ($B-R \gtrsim 0.5\,\mathrm{mag}$) 7 days after the explosion (see

the DDC20, DDC22, and DDC25 models in their Figure 1). However, these models never appear as blue as SN 2022joj, and the ^{56}Ni yields are relatively low ($M_{\mathrm{Ni56}} \lesssim 0.3\,\mathrm{M}_\odot$), so they would result in subluminous events. In addition, we do not know any multidimensional explosion models that fail to produce any ^{56}Ni mixing within the ejecta, and therefore disfavor this scenario.

Alternatively, in the double detonation scenario, a layer of IGEs in the ashes of the helium shell can produce significant opacity in the outer layers of the bulk ejecta, producing a red color (Polin et al. 2019). This scenario has been proposed for a few SNe with red colors at early times, including SN 2016jhr (Jiang et al. 2017) and SN 2018aoz (Ni et al. 2022). In Figure 7 we compare the spectra of SN 2022joj at −12 days and +3 days with 1D double detonation models from Polin et al. (2019) and 2D double detonation models from Shen et al. (2021b). To create synthetic spectra, both models use `Sedona` (Kasen et al. 2006), a multi-dimensional radiative transfer (RT) simulator that assumes local thermodynamical equilibrium (LTE).

In the 1D models, the most important parameters are the mass of the C/O core (M_c) and the mass of the helium shell (M_s). The maximum luminosity depends on the amount of ^{56}Ni synthesized in the explosion, which is predominantly determined by the total progenitor mass ($M_c + M_s$; Polin et al. 2019). We find that the maximum brightness in B band ($M_{B,\mathrm{max}} = -19.62\,\mathrm{mag}$) is reproduced by the 1D models with relatively massive progenitors (∼1.1–1.2 M$_\odot$). However, models with such massive progenitors tend to produce blue, featureless spectra at early times (e.g., the $M_c = 1.1\,\mathrm{M}_\odot$, $M_s = 0.05\,\mathrm{M}_\odot$ model in Figure 7), inconsistent with the observations. Less massive models provide a better match to the line-blanketing seen in the early spectra, but fail to reproduce the maximum brightness as well as the 4200 Å features in the observed spectra. The 1D models overestimate the pEW and the expansion velocity of the Si II λ6355 line at peak. As a reference, we overplot the theoretical $M_{B,\mathrm{max}}$-$v_{\mathrm{Si\,II}}$ relation of 1D double detonation models for thin helium shells ($M_s = 0.01\,M_\odot$) across a spectrum of progenitor masses in Polin et al. (2019) as the dashed black curve in the left panel of Figure 6, which is not in agreement with the properties of SN 2022joj.

While the 1D models do not fully reproduce the observed properties of SN 2022joj, some of these tensions can be resolved when considering viewing angle effects in multi-dimensional models. In Figure 6 we also show the properties of three 2D double detonation models from Shen et al. (2021b) with a variety of M_c and
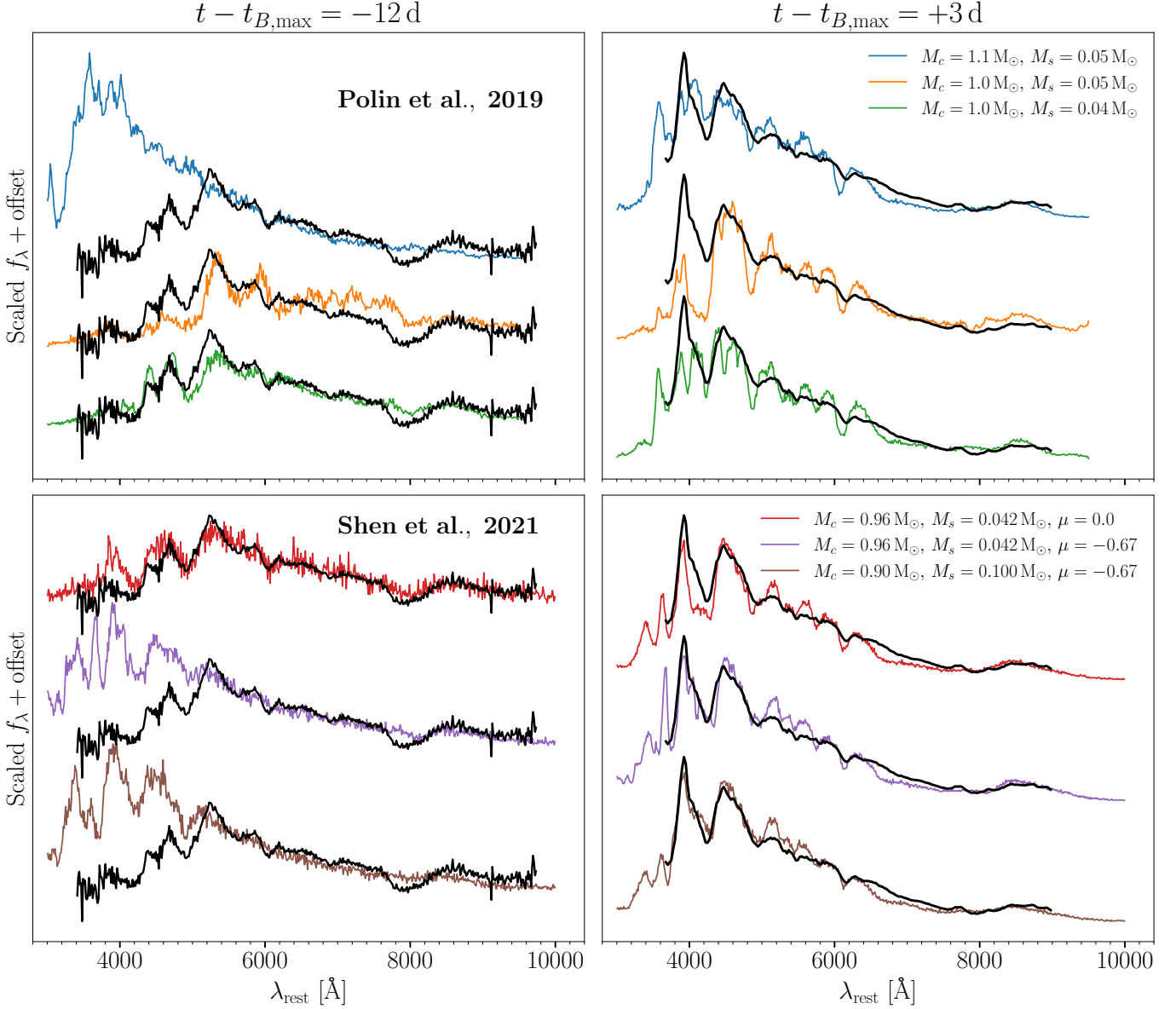
Figure 7. Comparisons of an early spectrum (−12 days) and a maximum-light spectrum (+3 days) of SN 2022joj (black) with two sets of double detonation models at corresponding phases. *Top:* results of 1D hydrodynamical simulations from Polin et al. (2019) with a variety of M_c and M_s. *Bottom:* results of 2D hydrodynamical simulations from (Shen et al. 2021b). A Galactic extinction of $E(B − V)_{\mathrm{MW}} = 0.032$ mag has been applied to each synthetic spectrum.

M_s.[16] For the consistency in comparing the synthetic brightness with the observations of SN 2022joj, of which the K-corrections are unknown, the synthetic fluxes in the B filter of these models are evaluated after shift-

---

[16] The $v_{\mathrm{Si\,II}}$ is systematically higher than the values displayed in the Figure 20 from Shen et al. (2021b). In Shen et al. (2021b), the $v_{\mathrm{Si\,II}}$ is determined using the minimum of the Si II λ6355 absorption without subtracting the continuum, such that the estimated minimum is systematically redshifted with respect to the actual line center, whereas we fit the absorption features with Gaussian profiles on top of a linear continuum.

ing the synthetic spectrum to $z = 0.02736$, the redshift of SN 2022joj. We obtain the Si II line properties using the same fitting techniques as in Section 3.3. We again find that more massive progenitors generally lead to more luminous SNe, but different viewing angles produce significantly different spectral properties as a result of the asymmetry of the ejecta – materials closer to the point of helium ignition are less dense and expand faster (Shen et al. 2021b). In the plot, the cosine value of the polar angle relative to the point of helium ignition, μ, ranges from +0.93 (near the helium ignition point) to −0.93 (opposite to the helium ignition point). When

the SN is observed along a line of sight closer to the detonation point in the shell (greater μ), it will appear fainter at maximum brightness and show a higher line velocity in Si II $\lambda 6355$. For a relatively high progenitor mass ($\gtrsim 1.1\,M_\odot$), a high $v_{\rm Si\,II}$ ($\gtrsim 13,500\,\rm km\,s^{-1}$) is predicted in 1D models. However, all the 2D models with $\mu \lesssim 0$ show a lower $v_{\rm Si\,II}$ ($\lesssim 12,000\,\rm km\,s^{-1}$), much closer to SN 2022joj in the $M_{B,\max}$-$v_{\rm Si\,II}$ phase space. Models with $\mu > 0$ are more consistent with 1D model predictions. It is suggested in Polin et al. (2019) that high-velocity SNe that follow the dashed line in Figure 6 result from sub-$M_{\rm Ch}$ double detonations, while SNe in the clump centered at $M_{B,\max} \simeq -19.5\,\rm mag$ and $v_{\rm Si\,II} \simeq 11,000\,\rm km\,s^{-1}$ are likely near-$M_{\rm Ch}$ explosions. Based on the 2D models, however, we should expect a similar number of high-velocity and normal-velocity double-detonation SNe Ia. A substantial fraction of the objects within the clump on the $M_{B,\max}$-$v_{\rm Si\,II}$ diagram may be sub-$M_{\rm Ch}$ double-detonation events viewed from certain orientations (Shen et al. 2021b). SN 2018aoz is a double-detonation candidate that, like SN 2022joj, exhibits early red colors before evolving to normal luminosity and blue colors (Ni et al. 2022). Interestingly, SN 2018aoz also resides in the high-luminosity, low-velocity clump in the $M_{B,\max}$-$v_{\rm Si\,II}$ space (Ni et al. 2023), and thus, it too may be an example of a double-detonation SN Ia viewed from the hemisphere opposite to the helium ignition point.

In the bottom panels of Figure 7 we show three 2D double detonation models with a total progenitor mass of $\sim 1\,M_\odot$ from Shen et al. (2021b). These models, particularly the $\mu = -0.67$ ones, qualitatively match the observed spectra at maximum light. In the $M_c = 0.96\,M_\odot$, $M_s = 0.042\,M_\odot$ model, we find that when $\mu = 0$ (viewed from the equator), it predicts a reasonable level of line blanketing in the blue side of the spectrum at early times (lower left panel of Figure 7). Near maximum brightness, the model also reproduces the overall shape of the observed spectrum, though the strength of nearly all the absorption lines (4200 Å features, S II, and Si II) is overestimated. $v_{\rm Si\,II}$ is also overestimated ($\sim 12,000\,\rm km\,s^{-1}$). When viewed from the hemisphere opposite the helium ignition point (e.g., $\mu = -0.67$), the model yields an asymmetric profile of 4200 Å features that matches the observations better. The Si II features are also predicted to be shallower, though still not as shallow as that in the observations. Nonetheless, the spectra at early times are expected to be much bluer than the observations. The $M_c = 0.90\,M_\odot$, $M_s = 0.100\,M_\odot$ model produces even shallower and slower-expanding Si II features at maximum brightness. This is in agreement with the trend observed in the right panel of Figure 6: models with a

thicker helium shell tend to exhibits shallower Si II features. However, the level of line-blanketing blueward of ~ 5000 Å is also underestimated at early times.

The extremely red near-UV colors near maximum luminosity are also broadly consistent with the double detonation scenario, since the heavy elements (e.g., Ti, V, Cr, and Fe) in the outer ejecta could effectively absorb the UV photons with wavelengths around 3000 Å. However, no existing models could accurately model the UVOT light curves, especially in the u-band (~ 3100–3900 Å in the observed frame, or ~ 3000–3800 Å in the rest frame of the host galaxy), where the flux is dominated by the re-emission of Ti, V, and Cr, and non-LTE effects could be important.

While none of the models presented here provide a strong match to SN 2022joj at every phase, we draw the broad conclusion that the spectroscopic properties of SN 2022joj are qualitatively consistent with a sub-$M_{\rm Ch}$ WD ($\gtrsim 1.0\,M_\odot$) double detonation viewed from the hemisphere opposite to the ignition point. Observers from such a viewing angle would observe strong absorption features in the blue portion of the spectrum dominated by IGEs as well as relatively shallow and slowly-expanding Si II lines in the red portion. We emphasize that none of the models considered here was specifically developed and tuned to explain SN 2022joj. Customized models specifically tuned for SN 2022joj may reproduce all the observed features simultaneously, and we suggest more 2D double detonation simulations be performed. Additional improvements can be made via an improved handling of the radiative transfer (e.g., non-LTE effects; see Shen et al. 2021a).

4.2. *The 7300 Å Region in Nebular-phase Spectra*

In Figure 8 we compare the two nebular-phase spectra of SN 2022joj with the overluminous SNe Ia (SN 1991T, SN 1999aa, and SN 2018cnw) and the normal luminosity SN 2011fe.

Compared to other SNe Ia, the nebular spectra of SN 2022joj show a relatively low flux ratio between the complex at ~ 7300 Å (hereafter the 7300 Å features) dominated by [Fe II] and [Ni II] and the complex at ~ 4700 Å dominated by [Fe III]. This suggests high ionization in the ejecta (Wilk et al. 2020). In addition to the smaller flux ratio, the profile of the 7300 Å features in SN 2022joj is also distinct from other SNe. Most of SNe Ia show a bimodal structure in their 7300 Å features (e.g., Graham et al. 2017; Maguire et al. 2018). The bluer peak is dominated by [Fe II] $\lambda\lambda 7155, 7172$, while [Ni II] $\lambda\lambda 7378, 7412$ usually have non-negligible contributions to the redder peak (see Figure 8). In some peculiar SNe Ia (mostly subluminous ones), the de-
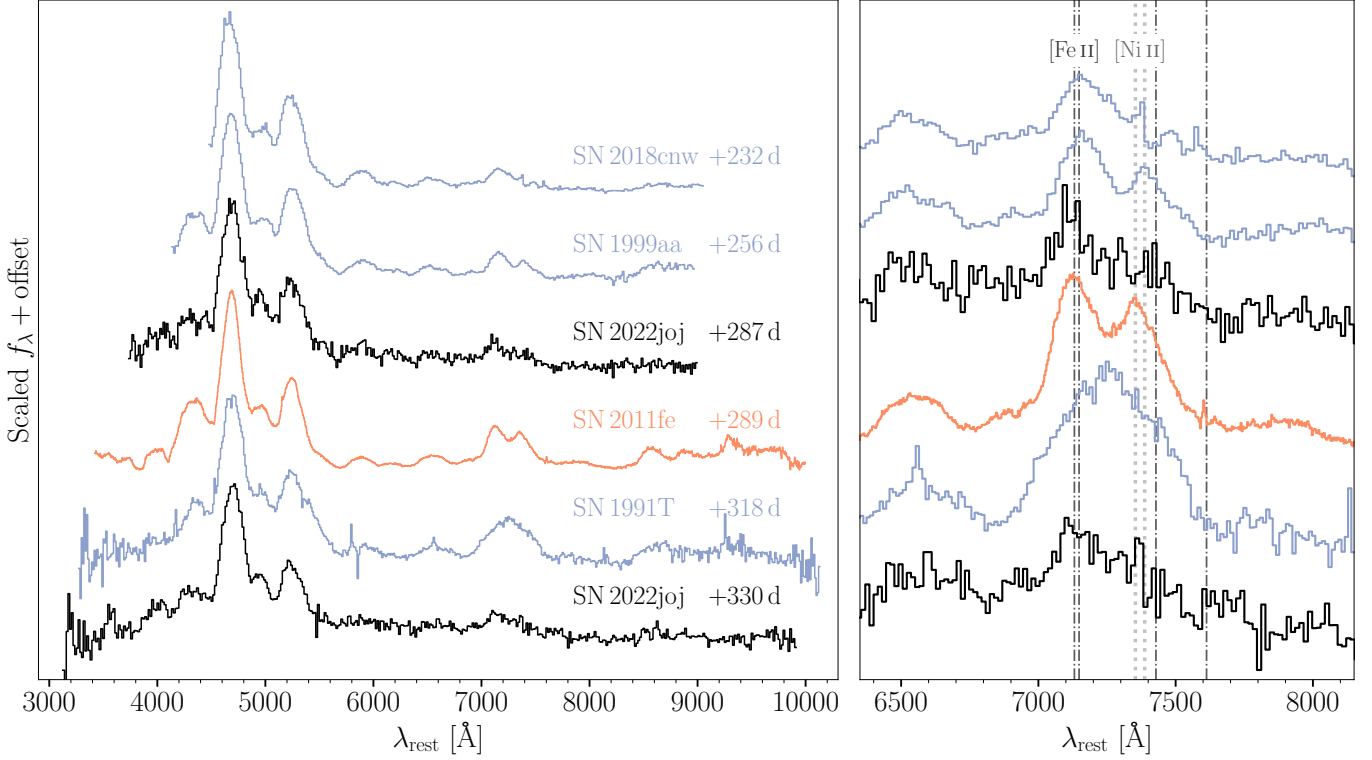
Figure 8. Nebular-phase spectra of SN 2022joj (black), three overluminous SNe Ia (blue), SN 1991T, SN 1999aa, and SN 2018cnw, and a normal SN Ia (orange), SN 2011fe. The right panel zooms in on the features around 7300 Å. The flux has been normalized to the [Fe III] features around 4700 Å. The dash-dotted lines correspond to wavelengths of four [Fe II] lines (7155 Å, 7172 Å, 7453 Å, and 7638 Å), while the dotted lines correspond to the wavelengths of two [Ni II] lines (7378 Å, 7412 Å), both blueshifted by $1000\,\mathrm{km\,s^{-1}}$. Spectra were downloaded from WiseREP (Yaron & Gal-Yam 2012), with the following original data sources: SN 1991T and SN 1999aa – Silverman et al. (2012); SN 2011fe – Mazzali et al. (2015); SN 2018cnw – this work.
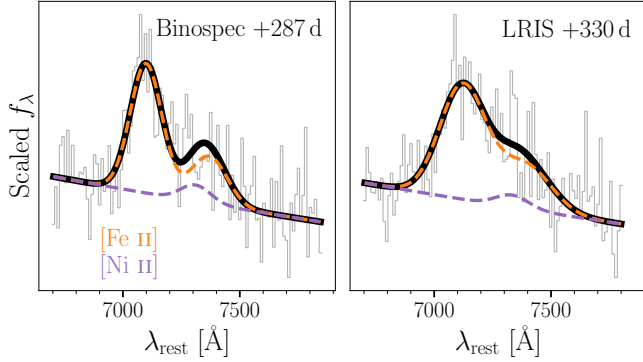
Figure 9. Fits to the 7300 Å region containing [Fe II] and [Ni II] features are consistent with a low Ni II abundance. The observed spectra are shown in grey. The dashed lines correspond to the models of [Fe II] (orange) and [Ni II] (purple) features. For the model parameters we adopt the mean values of their posterior distributions. The black solid lines are the overall models.

tection of [Ca II] $\lambda\lambda$7291, 7324 has also been reported (e.g. Jacobson-Galán et al. 2020; Siebert et al. 2020). The bimodal morphology is prominent in the spectra of SN 1999aa and SN 2011fe. SN 1999T is well-known

for its broader emission lines in the nebular phase, so the composition of the 7300 Å features is ambiguous. In the spectra of SN 2022joj and SN 2018cnw, however, the redder peak is absent and the 7300 Å features show an asymmetric single peak, which seems to indicate a low abundance of Ni in the ejecta.

To investigate the relative contributions of [Fe II] and [Ni II] to the 7300 Å features in SN 2022joj, we model this region with multiple Gaussian emission profiles using the same technique as in Section 3.3. We include four [Fe II] lines (7155, 7172, 7388, 7453 Å) and two [Ni II] lines (7378, 7412 Å) in the fit. For each species, the relative flux ratios of lines are fixed, whose values are adopted from Jerkstrand et al. (2015). For [Fe II], we set $L_{7155} : L_{7172} : L_{7388} : L_{7453} = 1 : 0.24 : 0.19 : 0.31$, and for [Ni II], we set $L_{7378} : L_{7412} = 1 : 0.31$. These line ratios are calculated assuming LTE, but the departure from LTE should not be significant under the typical conditions in the ejecta (Jerkstrand et al. 2015). We allow the amplitudes A of these Gaussian profiles to be either positive or negative. The velocity dispersions σ_v in different lines of each species are set to be the same. For both A and $\log \sigma_v$, we adopt flat pri-

ors. We only allow the σ_v to vary between 1000 and 6000 km s^{-1}. In addition, we adopt wide Gaussian priors for the radial velocities v of [Fe II] and [Ni II], both centered at -1000 km s^{-1} with a standard deviation of 2000 km s^{-1}. The fitted models are shown in Figure 9, where colored curves correspond to the [Fe II] and [Ni II] emission adopting the mean values of the posterior distributions of model parameters sampled with MCMC. The fitted parameters are listed in Table 6. In both spectra, the flux of [Ni II] is consistent with 0 ($L_{[\text{Ni II}] \lambda 7378}/L_{[\text{Fe II}] \lambda 7155} = 0.14 \pm 0.15$ at $+287$ days and 0.11 ± 0.12 at $+330$ days; the flux ratios of lines are estimated with the ratios of their pEWs, and the uncertainties are the robust standard deviations estimated with the median absolute deviation), and the 7300 Å features can be well fit with [Fe II] emission only. We have also tested fitting this complex with [Ca II] in addition to [Fe II] and [Ni II], but find no evidence for [Ca II].

The relative abundance of Ni and Fe, which probes the mass of the progenitor WD, can be estimated via the flux ratio of their emission lines. At >300 days after explosion ^{56}Fe is the dominant isotope of Fe following the decay of ^{56}Ni through the chain: ^{56}Ni$\rightarrow^{56}$Co$\rightarrow^{56}$Fe. Consequently, the Fe abundance primarily depends on the yield of ^{56}Ni. The Ni abundance, however, is sensitive to both the progenitor mass and the explosion scenario. The stable Ni isotopes (^{58}Ni, ^{60}Ni, and ^{62}Ni) are more neutron-rich compared to the α-species ^{56}Ni, and can only be formed in high-density regions with an enhanced electron capture rate during the explosion (Nomoto 1984; Khokhlov 1991). Consequently, SNe Ia from sub-M_{Ch} WDs, with central densities that are lower than near-M_{Ch} WDs, are expected to show a lower abundance of stable Ni isotopes (Iwamoto et al. 1999; Seitenzahl et al. 2013; Shen et al. 2018a).

To estimate the relative abundance of Ni and Fe, we use the equation adopted in Jerkstrand et al. (2015) and Maguire et al. (2018),

$$\frac{L_{7378}}{L_{7155}} = 4.9 \frac{n_{\text{Ni II}}}{n_{\text{Fe II}}} \exp\left(\frac{0.28\,\text{eV}}{k_B T}\right) \frac{dc_{\text{Ni II}}}{dc_{\text{Fe II}}}, \quad (1)$$

where L_{7378}/L_{7155} is the flux ratio of the [Ni II] $\lambda 7378$ to [Fe II] $\lambda 7155$ lines, $n_{\text{Ni II}}/n_{\text{Fe II}}$ is the number density ratio of Ni II and Fe II, and $dc_{\text{Ni II}}/dc_{\text{Fe II}}$ is the ratio of the departure coefficients from LTE for these two ions. Since both Ni II and Fe II are singly ionized species with similar ionization potentials, we assume that $n_{\text{Ni II}}/n_{\text{Fe II}}$ is a good approximation of the total Ni/Fe ratio. As is illustrated in Maguire et al. (2018), this assumption proves to be valid by modeling nebular phase spectra at similar phases (Fransson & Jerkstrand 2015; Shingles et al. 2022), with the relative deviation from the

ionization balance $\lesssim 20\%$. We handle the uncertainties due to the unknown temperature, ratio of departure coefficients, and the ionization balance in a Monte Carlo way. We randomly generate $N = 4000$ samples of the temperature (3000–8000 K), the ratio of departure coefficients (1.2–2.4), and the ionization balance factor (0.8–1.2) assuming uncorrelated uniform distributions. These intervals are again adopted from Maguire et al. (2018). Combining these quantities with the samples of line profile parameters drawn with the MCMC, we obtain N estimates of Ni/Fe, which are effectively drawn from its posterior distribution. We find that Ni/Fe is consistent with 0 and we obtain a 3-σ upper limit of Ni/Fe < 0.03. Such a low Ni abundance is more consistent with the yields of sub-M_{Ch} double detonation scenarios (Shen et al. 2018a), much lower than the expected outcomes of near-M_{Ch}, delayed detonation models (Seitenzahl et al. 2013) or pure deflagration models (Iwamoto et al. 1999).

Alternatively, it is proposed in Blondin et al. (2022) that for high-luminosity SNe Ia, the absence of [Ni II] lines can be a result of high ionization of Ni in the inner ejecta, despite the fact that a significant amount of Ni exists. It is shown that the [Ni II] $\lambda\lambda 7378, 7412$ lines can be strongly suppressed even in a high-luminosity, near-M_{Ch} delayed-detonation model, once the Ni II/Ni III ratio at the center of the ejecta is artificially reduced by a factor of 10. Nevertheless, it remains to be questioned whether a physical mechanism exists to boost the ionization in the inner ejecta, where the stable Ni dominates the radioactive ^{56}Ni and ^{56}Co, and the deposited energy per particle due to the radioactive decay is usually low. One possible scenario is inward mixing, which brings ^{56}Co into the innermost ejecta such that the ionization would significantly increase. However, in this case calcium would inevitably be mixed inward as well, and the resultant Ca II $\lambda\lambda 7291, 7324$ lines would stand out and dominate the 7300 Å features (Blondin et al. 2022). Other physical mechanism are thus required to reduce the Ni II/Ni III ratio at the center of a near-M_{Ch} explosion.

We also find that the [Fe II] lines are significantly blueshifted ($v_{[\text{Fe II}]} = -(2.49 \pm 0.38) \times 10^3$ km s^{-1} at $+287$ days and $-(1.47 \pm 0.62) \times 10^3$ km s^{-1} at $+330$ days). This is consistent with other SNe Ia showing low $v_{\text{Si II}}$ at maximum brightness (Maeda et al. 2010b; Maguire et al. 2018; Li et al. 2021), and also in qualitative agreement with the asymmetric sub-M_{Ch} double detonation scenario. Specifically, along a line of sight opposite to the shell detonation point, observers would see intermediate mass elements (IMEs) with low expansion velocities, including Si II. In the meantime, the IGEs at the center

of the ejecta would have a bulk velocity towards the observer (see Figure 1 and Figure 2 in Bulla et al. 2016; see also Fink et al. 2010).

4.3. *Carbon in the Pre-maximum Spectra*

At the late stage of preparing this work, three additional spectra obtained by LCO between -7 days and $+2$ days were made public after the proprietary period, which exhibit strong C II $\lambda\lambda6580, 7234$ lines. Interestingly, in the earliest spectrum at -12 days, there is no evidence for these C II lines, indicating that a significant amount of carbon is located in the interior ejecta, with little carbon on the surface.

In double detonations of sub-$M_{\rm Ch}$ WDs, the burning of carbon is expected to be efficient, with only a small fraction of carbon left unburnt. In 1D double detonation models from Polin et al. (2019), only a negligible ($\lesssim 10^{-5}\,M_\odot$) amount of carbon is unburnt in normal and overluminous SNe, which should not cause any noticeable spectroscopic features. Multidimensional simulations could alleviate this tension. A greater amount ($\sim 10^{-4}$–$10^{-3}\,M_\odot$) of leftover carbon is predicted in 2D double detonation models (Fink et al. 2010; Boos et al. 2021), which is still roughly two orders of magnitude lower than the yields of IMEs. Nevertheless, most of the unburnt carbon will be concentrated on the surface of the C/O core, forming a sharp carbon-rich shell (see Figure 5–8 in Boos et al. 2021). This is in qualitative agreement with the delayed appearance of the C II features in the spectral evolution, since both 1D and 2D double detonation models produce little carbon in the helium ashes. The carbon features may only be visible at later times, when the photosphere moves inward to the carbon-rich regions. Nevertheless, with the current resolution in the RT simulations, the contribution of such a sharp shell is unlikely to be captured in the resultant synthetic spectra.

Another possible origin of carbon in a double-detonation SN is the stripped material from a degenerate companion. In the Dynamically Driven Double-Degenerate Double-Detonation (D^6) model (Shen et al. 2018b), the primary C/O WD could detonate following the dynamical ignition of a helium shell from its WD companion (either a helium WD or a C/O WD with a substantial helium envelope) during the unstable mass transfer (Guillochon et al. 2010; Pakmor et al. 2013). In this case, a significant amount ($\sim 10^{-3}\,M_\odot$) of materials can be stripped from a C/O WD companion, following the explosion of a $1\,M_\odot$ primary WD (Tanikawa et al. 2018; Boos et al. 2023, in prep.), although the amount of carbon would likely to be significantly less if the companion still holds a substantial helium envelope (Tanikawa et al. 2019).

Explosion mechanisms that would result in a greater amount of unburnt carbon in the ejecta include the pure deflagration (Nomoto et al. 1984) or pulsating delayed detonation (Hoeflich et al. 1995; Dessart et al. 2014) of a near-$M_{\rm Ch}$ WD, and the violent merger of binary WDs (Raskin et al. 2014). None of these models could produce the unusual red color in the early light curves or the peculiar spectroscopic features of SN 2022joj equally well as the helium-shell double detonation scenario does. In addition, customized modifications will have to be made to these models to explain the deferred occurrence of C II features.

We conclude that while it remains to be questioned if double detonations could really produce strong carbon features, the detection of strong C II $\lambda\lambda6580, 7234$ lines in SN 2022joj does not necessarily invalidate our hypothesis of its double-detonation origin.

5. CONCLUSIONS

We have presented observations of SN 2022joj, a peculiar SN Ia. SN 2022joj has an unusual color evolution, with a remarkably red $g_{\rm ZTF} - r_{\rm ZTF}$ color at early times due to continuous absorption in the blue portion of its spectral energy distribution. Absorption features observed around maximum light simultaneously suggest high (a blue continuum and shallow Si II lines similar to those of overluminous, 99aa-/91T-like SNe) and low (strong absorption around 4200 Å resembling the Ti-trough in subluminous, 91bg-like SNe) photospheric temperatures. The nebular-phase spectra of SN 2022joj suggest a high ionization and low Ni abundance in the ejecta, consistent with a sub-$M_{\rm Ch}$ explosion.

The early red colors are most likely due to a layer of IGEs in the outermost ejecta as products of a helium-shell detonation, in the sub-$M_{\rm Ch}$ double detonation scenario. If the asymmetric ejecta are observed from the hemisphere opposite to the helium ignition point, we find that the resultant synthetic spectra could qualitatively reproduce some of the observed properties, including (i) significant line-blanketing of flux due to IGEs at early phases; (ii) strong absorption features around 4200 Å as well as relatively weak Si II features near maximum brightness, and (iii) blueshifted [Fe II] $\lambda7155$ accompanied with a relatively low expansion velocity of Si II at peak. No existing double detonation model can fully explain all the observational properties of SN 2022joj. As a result, it is possible that some alternative model is superior, though we find the early red colors are difficult to explain with any other alternative

Table 6. Fits to the late-time spectra around 7300 Å with [Fe II] and [Ni II] emission.

Phase	[Fe II] λ7155			[Ni II] λ7378		
	v	σ_v	pEW	v	σ_v	pEW
(day)	$(10^3\,\mathrm{km\,s^{-1}})$	$(10^3\,\mathrm{km\,s^{-1}})$	(Å)	$(10^3\,\mathrm{km\,s^{-1}})$	$(10^3\,\mathrm{km\,s^{-1}})$	(Å)
+286.8	-2.49 ± 0.38	2.88 ± 0.45	-122 ± 21	-3.04 ± 2.69	2.92 ± 1.44	-14 ± 19
+329.8	-1.47 ± 0.62	4.24 ± 0.77	-130 ± 27	-2.09 ± 2.24	3.17 ± 1.48	-9 ± 21

explosion scenario. Future 2D models covering a finer grid of progenitor properties may answer the question if SN 2022joj is really a peculiar SN triggered by a double detonation.

Facility: PO:1.2m (ZTF), Swift (UVOT), Liverpool:2m (IO:O), KAIT, PO:1.5m (SEDM), FTN (FLOYDS), FTS (FLOYDS), NOT (ALFOSC), Liverpool:2m (SPRAT), Keck:I (LRIS), MMT (Binospec).

Software: astropy (Astropy Collaboration et al. 2013, 2018), dynesty (Speagle 2020b), matplotlib (Hunter 2007), NumPy (Harris et al. 2020), prospector (Johnson et al. 2021b), PyMC (Salvatier et al. 2016), PypeIt (Prochaska et al. 2020), pysedm (Rigault et al. 2019), SALT3 (Kenworthy et al. 2021), sncosmo (Barbary et al. 2023), TARDIS (Kerzendorf & Sim 2014; Kerzendorf et al. 2019), Python-FSPS (Conroy et al. 2009b; Conroy & Gunn 2010; Foreman-Mackey et al. 2014).

REFERENCES

Aihara, H., Armstrong, R., Bickerton, S., et al. 2018, PASJ, 70, S8, doi: 10.1093/pasj/psx081

Arbour, R., Papenkova, M., Li, W. D., Filippenko, A. V., & Armstrong, M. 1999, IAUC, 7156, 1

Astropy Collaboration, Robitaille, T. P., Tollerud, E. J., et al. 2013, A&A, 558, A33, doi: 10.1051/0004-6361/201322068

Astropy Collaboration, Price-Whelan, A. M., Sipőcz, B. M., et al. 2018, AJ, 156, 123, doi: 10.3847/1538-3881/aabc4f

Barbary, K., Bailey, S., Barentsen, G., et al. 2023, SNCosmo, v2.10.0, Zenodo, doi: 10.5281/zenodo.7876632

Bellm, E. C., Kulkarni, S. R., Graham, M. J., et al. 2019a, PASP, 131, 018002, doi: 10.1088/1538-3873/aaecbe

Bellm, E. C., Kulkarni, S. R., Barlow, T., et al. 2019b, PASP, 131, 068003, doi: 10.1088/1538-3873/ab0c2a

Blagorodnova, N., Neill, J. D., Walters, R., et al. 2018, PASP, 130, 035003, doi: 10.1088/1538-3873/aaa53f

Blondin, S., Bravo, E., Timmes, F. X., Dessart, L., & Hillier, D. J. 2022, A&A, 660, A96, doi: 10.1051/0004-6361/202142323

Blondin, S., & Tonry, J. L. 2007, ApJ, 666, 1024, doi: 10.1086/520494

Boos, S. J., Townsley, D. M., Shen, K. J., Caldwell, S., & Miles, B. J. 2021, ApJ, 919, 126, doi: 10.3847/1538-4357/ac07a2

Branch, D., Thomas, R. C., Baron, E., et al. 2004, ApJ, 606, 413, doi: 10.1086/382950

Branch, D., Dang, L. C., Hall, N., et al. 2006, PASP, 118, 560, doi: 10.1086/502778

Brown, P. J., Perry, J. M., Beeny, B. A., Milne, P. A., & Wang, X. 2018, ApJ, 867, 56, doi: 10.3847/1538-4357/aae1ad

Brown, T. M., Baliber, N., Bianco, F. B., et al. 2013, PASP, 125, 1031, doi: 10.1086/673168

Bulla, M., Sim, S. A., Kromer, M., et al. 2016, MNRAS, 462, 1039, doi: 10.1093/mnras/stw1733

Bulla, M., Miller, A. A., Yao, Y., et al. 2020, ApJ, 902, 48, doi: 10.3847/1538-4357/abb13c

Burrow, A., Baron, E., Ashall, C., et al. 2020, ApJ, 901, 154, doi: 10.3847/1538-4357/abafa2

Byler, N., Dalcanton, J. J., Conroy, C., & Johnson, B. D. 2017, ApJ, 840, 44, doi: 10.3847/1538-4357/aa6c66

Calzetti, D., Armus, L., Bohlin, R. C., et al. 2000, ApJ, 533, 682, doi: 10.1086/308692

Carrick, J., Turnbull, S. J., Lavaux, G., & Hudson, M. J. 2015, MNRAS, 450, 317, doi: 10.1093/mnras/stv547

Cenko, S. B., Fox, D. B., Moon, D.-S., et al. 2006, PASP, 118, 1396, doi: 10.1086/508366

Chabrier, G. 2003, PASP, 115, 763, doi: 10.1086/376392

Childress, M. J., Filippenko, A. V., Ganeshalingam, M., & Schmidt, B. P. 2014, MNRAS, 437, 338, doi: 10.1093/mnras/stt1892

Childress, M. J., Scalzo, R. A., Sim, S. A., et al. 2013, ApJ, 770, 29, doi: 10.1088/0004-637X/770/1/29

Chu, M., Dahiwale, A., & Fremling, C. 2022, Transient Name Server Classification Report, 2022-1458, 1

Conroy, C. 2013, ARA&A, 51, 393, doi: 10.1146/annurev-astro-082812-141017

Conroy, C., & Gunn, J. E. 2010, ApJ, 712, 833, doi: 10.1088/0004-637X/712/2/833

Conroy, C., Gunn, J. E., & White, M. 2009a, ApJ, 699, 486, doi: 10.1088/0004-637X/699/1/486

—. 2009b, ApJ, 699, 486, doi: 10.1088/0004-637X/699/1/486

De, K., Kasliwal, M. M., Polin, A., et al. 2019, ApJ, 873, L18, doi: 10.3847/2041-8213/ab0aec

De, K., Kasliwal, M. M., Tzanidakis, A., et al. 2020, ApJ, 905, 58, doi: 10.3847/1538-4357/abb45c

de los Reyes, M. A. C., Kirby, E. N., Seitenzahl, I. R., & Shen, K. J. 2020, ApJ, 891, 85, doi: 10.3847/1538-4357/ab736f

Dekany, R., Smith, R. M., Riddle, R., et al. 2020, PASP, 132, 038001, doi: 10.1088/1538-3873/ab4ca2

Dessart, L., Blondin, S., Hillier, D. J., & Khokhlov, A. 2014, MNRAS, 441, 532, doi: 10.1093/mnras/stu598

Dey, A., Schlegel, D. J., Lang, D., et al. 2019, AJ, 157, 168, doi: 10.3847/1538-3881/ab089d

Dong, Y., Valenti, S., Polin, A., et al. 2022, ApJ, 934, 102, doi: 10.3847/1538-4357/ac75eb

Duev, D. A., Mahabal, A., Masci, F. J., et al. 2019, MNRAS, 489, 3582, doi: 10.1093/mnras/stz2357

Eitner, P., Bergemann, M., Ruiter, A. J., et al. 2022, arXiv e-prints, arXiv:2206.10258. https://arxiv.org/abs/2206.10258

El-Badry, K., Shen, K. J., Chandra, V., et al. 2023, arXiv e-prints, arXiv:2306.03914, doi: 10.48550/arXiv.2306.03914

Fabricant, D., Fata, R., Epps, H., et al. 2019, PASP, 131, 075004, doi: 10.1088/1538-3873/ab1d78

Filippenko, A. V., Richmond, M. W., Matheson, T., et al. 1992a, ApJL, 384, L15, doi: 10.1086/186252

Filippenko, A. V., Richmond, M. W., Branch, D., et al. 1992b, AJ, 104, 1543, doi: 10.1086/116339

Fink, M., Röpke, F. K., Hillebrandt, W., et al. 2010, A&A, 514, A53, doi: 10.1051/0004-6361/200913892

Fitzpatrick, E. L. 1999, PASP, 111, 63, doi: 10.1086/316293

Flörs, A., Spyromilio, J., Taubenberger, S., et al. 2020, MNRAS, 491, 2902, doi: 10.1093/mnras/stz3013

Foreman-Mackey, D., Sick, J., & Johnson, B. 2014, Python-Fsps: Python Bindings To Fsps (V0.1.1), v0.1.1, Zenodo, doi: 10.5281/zenodo.12157

Fransson, C., & Jerkstrand, A. 2015, ApJL, 814, L2, doi: 10.1088/2041-8205/814/1/L2

Fremling, C. 2022, Transient Name Server Discovery Report, 2022-1220, 1

Galbany, L., Ashall, C., Hflich, P., et al. 2019, A&A, 630, A76, doi: 10.1051/0004-6361/201935537

Garavini, G., Folatelli, G., Goobar, A., et al. 2004, AJ, 128, 387, doi: 10.1086/421747

Gehrels, N., Chincarini, G., Giommi, P., et al. 2004, ApJ, 611, 1005, doi: 10.1086/422091

Graham, M. J., Kulkarni, S. R., Bellm, E. C., et al. 2019, PASP, 131, 078001, doi: 10.1088/1538-3873/ab006c

Graham, M. L., Kumar, S., Hosseinzadeh, G., et al. 2017, MNRAS, 472, 3437, doi: 10.1093/mnras/stx2224

Guillochon, J., Dan, M., Ramirez-Ruiz, E., & Rosswog, S. 2010, ApJL, 709, L64, doi: 10.1088/2041-8205/709/1/L64

Harris, C. R., Millman, K. J., van der Walt, S. J., et al. 2020, Nature, 585, 357, doi: 10.1038/s41586-020-2649-2

HEASARC. 2014, HEAsoft: Unified Release of FTOOLS and XANADU, Astrophysics Source Code Library, record ascl:1408.004. http://ascl.net/1408.004

Hoeflich, P., Khokhlov, A. M., & Wheeler, J. C. 1995, ApJ, 444, 831, doi: 10.1086/175656

Hunter, J. D. 2007, Computing in Science and Engineering, 9, 90, doi: 10.1109/MCSE.2007.55

Inserra, C., Sim, S. A., Wyrzykowski, L., et al. 2015, ApJL, 799, L2, doi: 10.1088/2041-8205/799/1/L2

Iwamoto, K., Brachwitz, F., Nomoto, K., et al. 1999, ApJS, 125, 439, doi: 10.1086/313278

Jacobson-Galán, W. V., Polin, A., Foley, R. J., et al. 2020, ApJ, 896, 165, doi: 10.3847/1538-4357/ab94b8

Jerkstrand, A., Smartt, S. J., Sollerman, J., et al. 2015, MNRAS, 448, 2482, doi: 10.1093/mnras/stv087

Jiang, J.-a., Doi, M., Maeda, K., et al. 2017, Nature, 550, 80, doi: 10.1038/nature23908

Johnson, B. D., Leja, J., Conroy, C., & Speagle, J. S. 2021a, ApJS, 254, 22, doi: 10.3847/1538-4365/abef67

—. 2021b, ApJS, 254, 22, doi: 10.3847/1538-4365/abef67

Kasen, D. 2010, ApJ, 708, 1025, doi: 10.1088/0004-637X/708/2/1025

Kasen, D., Thomas, R. C., & Nugent, P. 2006, ApJ, 651, 366, doi: 10.1086/506190

Kasen, D., Nugent, P., Wang, L., et al. 2003, ApJ, 593, 788, doi: 10.1086/376601

Kenworthy, W. D., Jones, D. O., Dai, M., et al. 2021, ApJ, 923, 265, doi: 10.3847/1538-4357/ac30d8

Kerzendorf, W., Nbauer, U., Sim, S., et al. 2019, tardis-sn/tardis: TARDIS v3.0 alpha2, doi: 10.5281/zenodo.2590539

Kerzendorf, W. E., & Sim, S. A. 2014, MNRAS, 440, 387, doi: 10.1093/mnras/stu055

Khokhlov, A. M. 1991, A&A, 245, L25

Kirby, E. N., Xie, J. L., Guo, R., et al. 2019, ApJ, 881, 45, doi: 10.3847/1538-4357/ab2c02

Kromer, M., Sim, S. A., Fink, M., et al. 2010, ApJ, 719, 1067, doi: 10.1088/0004-637X/719/2/1067

Leibundgut, B., Kirshner, R. P., Phillips, M. M., et al. 1993, AJ, 105, 301, doi: 10.1086/116427

Li, W., Wang, X., Bulla, M., et al. 2021, ApJ, 906, 99, doi: 10.3847/1538-4357/abc9b5

Lira, P. 1996, Master's thesis, -

Liu, C., Miller, A. A., Polin, A., et al. 2023a, ApJ, 946, 83, doi: 10.3847/1538-4357/acbb5e

Liu, Z.-W., Roepke, F. K., & Han, Z. 2023b, arXiv e-prints, arXiv:2305.13305, doi: 10.48550/arXiv.2305.13305

Livne, E. 1990, ApJL, 354, L53, doi: 10.1086/185721

Livne, E., & Arnett, D. 1995, ApJ, 452, 62, doi: 10.1086/176279

Maeda, K., Taubenberger, S., Sollerman, J., et al. 2010a, ApJ, 708, 1703, doi: 10.1088/0004-637X/708/2/1703

Maeda, K., Benetti, S., Stritzinger, M., et al. 2010b, Nature, 466, 82, doi: 10.1038/nature09122

Magee, M. R., & Maguire, K. 2020, A&A, 642, A189, doi: 10.1051/0004-6361/202037870

Magee, M. R., Maguire, K., Kotak, R., & Sim, S. A. 2021, MNRAS, 502, 3533, doi: 10.1093/mnras/stab201

Maguire, K., Sullivan, M., Pan, Y. C., et al. 2014, MNRAS, 444, 3258, doi: 10.1093/mnras/stu1607

Maguire, K., Sim, S. A., Shingles, L., et al. 2018, MNRAS, 477, 3567, doi: 10.1093/mnras/sty820

Mahabal, A., Rebbapragada, U., Walters, R., et al. 2019, PASP, 131, 038002, doi: 10.1088/1538-3873/aaf3fa

Maoz, D., Mannucci, F., & Nelemans, G. 2014, ARA&A, 52, 107, doi: 10.1146/annurev-astro-082812-141031

Masci, F. J., Laher, R. R., Rusholme, B., et al. 2023, arXiv e-prints, arXiv:2305.16279, doi: 10.48550/arXiv.2305.16279

—. 2019, PASP, 131, 018003, doi: 10.1088/1538-3873/aae8ac

Matheson, T., Kirshner, R. P., Challis, P., et al. 2008, AJ, 135, 1598, doi: 10.1088/0004-6256/135/4/1598

Mazzali, P. A., Chugai, N., Turatto, M., et al. 1997, MNRAS, 284, 151, doi: 10.1093/mnras/284.1.151

Mazzali, P. A., Sullivan, M., Filippenko, A. V., et al. 2015, MNRAS, 450, 2631, doi: 10.1093/mnras/stv761

Miller, A. A., Yao, Y., Bulla, M., et al. 2020, ApJ, 902, 47, doi: 10.3847/1538-4357/abb13b

Motohara, K., Maeda, K., Gerardy, C. L., et al. 2006, ApJL, 652, L101, doi: 10.1086/509919

Newsome, M., Li, W., Burke, J., et al. 2022, Transient Name Server Classification Report, 2022-1274, 1

Ni, Y. Q., Moon, D.-S., Drout, M. R., et al. 2022, Nature Astronomy, 6, 568, doi: 10.1038/s41550-022-01603-4

—. 2023, ApJ, 946, 7, doi: 10.3847/1538-4357/aca9be

Noebauer, U. M., Kromer, M., Taubenberger, S., et al. 2017, MNRAS, 472, 2787, doi: 10.1093/mnras/stx2093

Nomoto, K. 1982a, ApJ, 253, 798, doi: 10.1086/159682

—. 1982b, ApJ, 257, 780, doi: 10.1086/160031

—. 1984, ApJ, 277, 791, doi: 10.1086/161749

Nomoto, K., Thielemann, F. K., & Yokoi, K. 1984, ApJ, 286, 644, doi: 10.1086/162639

Nugent, P. E., Sullivan, M., Cenko, S. B., et al. 2011, Nature, 480, 344, doi: 10.1038/nature10644

Oke, J. B., Cohen, J. G., Carr, M., et al. 1995, PASP, 107, 375, doi: 10.1086/133562

Padilla Gonzalez, E., Howell, D. A., Burke, J., et al. 2023, arXiv e-prints, arXiv:2305.07708, doi: 10.48550/arXiv.2305.07708

Pakmor, R., Kromer, M., Taubenberger, S., & Springel, V. 2013, ApJL, 770, L8, doi: 10.1088/2041-8205/770/1/L8

Patat, F., Höflich, P., Baade, D., et al. 2012, A&A, 545, A7, doi: 10.1051/0004-6361/201219146

Patterson, M. T., Bellm, E. C., Rusholme, B., et al. 2019, PASP, 131, 018001, doi: 10.1088/1538-3873/aae904

Pereira, R., Thomas, R. C., Aldering, G., et al. 2013, A&A, 554, A27, doi: 10.1051/0004-6361/201221008

Phillips, A. C., Miller, J., Cowley, D., & Wallace, V. 2006, in Society of Photo-Optical Instrumentation Engineers (SPIE) Conference Series, Vol. 6269, Society of Photo-Optical Instrumentation Engineers (SPIE) Conference Series, ed. I. S. McLean & M. Iye, 62691O, doi: 10.1117/12.672469

Phillips, M. M., Lira, P., Suntzeff, N. B., et al. 1999, AJ, 118, 1766, doi: 10.1086/301032

Piascik, A. S., Steele, I. A., Bates, S. D., et al. 2014, in Society of Photo-Optical Instrumentation Engineers (SPIE) Conference Series, Vol. 9147, Ground-based and Airborne Instrumentation for Astronomy V, ed. S. K. Ramsay, I. S. McLean, & H. Takami, 91478H, doi: 10.1117/12.2055117

Piro, A. L., & Morozova, V. S. 2016, ApJ, 826, 96, doi: 10.3847/0004-637X/826/1/96

Piro, A. L., & Nakar, E. 2013, ApJ, 769, 67, doi: 10.1088/0004-637X/769/1/67

Polin, A., Nugent, P., & Kasen, D. 2019, ApJ, 873, 84, doi: 10.3847/1538-4357/aafb6a

Poole, T. S., Breeveld, A. A., Page, M. J., et al. 2008, MNRAS, 383, 627, doi: 10.1111/j.1365-2966.2007.12563.x

Prochaska, J. X., Hennawi, J. F., Westfall, K. B., et al. 2020, Journal of Open Source Software, 5, 2308, doi: 10.21105/joss.02308

Prochaska, J. X., Hennawi, J., Cooke, R., et al. 2020, pypeit/PypeIt: Release 1.0.0, v1.0.0, Zenodo, doi: 10.5281/zenodo.3743493

Raskin, C., Kasen, D., Moll, R., Schwab, J., & Woosley, S. 2014, ApJ, 788, 75, doi: 10.1088/0004-637X/788/1/75

Rigault, M., Neill, J. D., Blagorodnova, N., et al. 2019, A&A, 627, A115, doi: 10.1051/0004-6361/201935344

Roming, P. W. A., Kennedy, T. E., Mason, K. O., et al. 2005, SSRv, 120, 95, doi: 10.1007/s11214-005-5095-4

Ruiter, A. J., Belczynski, K., Sim, S. A., et al. 2011, MNRAS, 417, 408, doi: 10.1111/j.1365-2966.2011.19276.x

Ruiter, A. J., Belczynski, K., Sim, S. A., Seitenzahl, I. R., & Kwiatkowski, D. 2014, MNRAS, 440, L101, doi: 10.1093/mnrasl/slu030

Salvatier, J., Wiecki, T. V., & Fonnesbeck, C. 2016, PeerJ Computer Science, 2, e55, doi: 10.7717/peerj-cs.55

Sanders, J. L., Belokurov, V., & Man, K. T. F. 2021, MNRAS, 506, 4321, doi: 10.1093/mnras/stab1951

Schlafly, E. F., & Finkbeiner, D. P. 2011, ApJ, 737, 103, doi: 10.1088/0004-637X/737/2/103

Schulze, S., Krühler, T., Leloudas, G., et al. 2018, MNRAS, 473, 1258, doi: 10.1093/mnras/stx2352

Schulze, S., Yaron, O., Sollerman, J., et al. 2021, ApJS, 255, 29, doi: 10.3847/1538-4365/abff5e

Seitenzahl, I. R., Ciaraldi-Schoolmann, F., Röpke, F. K., et al. 2013, MNRAS, 429, 1156, doi: 10.1093/mnras/sts402

Shen, K. J., Blondin, S., Kasen, D., et al. 2021a, ApJL, 909, L18, doi: 10.3847/2041-8213/abe69b

Shen, K. J., Boos, S. J., Townsley, D. M., & Kasen, D. 2021b, ApJ, 922, 68, doi: 10.3847/1538-4357/ac2304

Shen, K. J., Kasen, D., Miles, B. J., & Townsley, D. M. 2018a, ApJ, 854, 52, doi: 10.3847/1538-4357/aaa8de

Shen, K. J., Boubert, D., Gänsicke, B. T., et al. 2018b, ApJ, 865, 15, doi: 10.3847/1538-4357/aad55b

Shingles, L. J., Flörs, A., Sim, S. A., et al. 2022, MNRAS, 512, 6150, doi: 10.1093/mnras/stac902

Siebert, M. R., Dimitriadis, G., Polin, A., & Foley, R. J. 2020, ApJL, 900, L27, doi: 10.3847/2041-8213/abae6e

Silverman, J. M., Foley, R. J., Filippenko, A. V., et al. 2012, MNRAS, 425, 1789, doi: 10.1111/j.1365-2966.2012.21270.x

Smith, K. W., Smartt, S. J., Young, D. R., et al. 2020, PASP, 132, 085002, doi: 10.1088/1538-3873/ab936e

Speagle, J. S. 2020a, MNRAS, 493, 3132, doi: 10.1093/mnras/staa278

—. 2020b, MNRAS, 493, 3132, doi: 10.1093/mnras/staa278

Steele, I. A., Smith, R. J., Rees, P. C., et al. 2004, in Society of Photo-Optical Instrumentation Engineers (SPIE) Conference Series, Vol. 5489, Ground-based Telescopes, ed. J. Oschmann, Jacobus M., 679–692, doi: 10.1117/12.551456

Tanikawa, A., Nomoto, K., & Nakasato, N. 2018, ApJ, 868, 90, doi: 10.3847/1538-4357/aae9ee

Tanikawa, A., Nomoto, K., Nakasato, N., & Maeda, K. 2019, ApJ, 885, 103, doi: 10.3847/1538-4357/ab46b6

Taubenberger, S. 2017, in Handbook of Supernovae, ed. A. W. Alsabti & P. Murdin (Springer), 317, doi: 10.1007/978-3-319-21846-5_37

Tonry, J. L., Denneau, L., Heinze, A. N., et al. 2018, PASP, 130, 064505, doi: 10.1088/1538-3873/aabadf

Townsley, D. M., Miles, B. J., Shen, K. J., & Kasen, D. 2019, ApJL, 878, L38, doi: 10.3847/2041-8213/ab27cd

Wang, L., & Wheeler, J. C. 2008, ARA&A, 46, 433, doi: 10.1146/annurev.astro.46.060407.145139

Wang, L., Baade, D., Höflich, P., et al. 2003, ApJ, 591, 1110, doi: 10.1086/375444

Wilk, K. D., Hillier, D. J., & Dessart, L. 2020, MNRAS, 494, 2221, doi: 10.1093/mnras/staa640

Woosley, S. E., Taam, R. E., & Weaver, T. A. 1986, ApJ, 301, 601, doi: 10.1086/163926

Woosley, S. E., & Weaver, T. A. 1994, ApJ, 423, 371, doi: 10.1086/173813

Yao, Y., Miller, A. A., Kulkarni, S. R., et al. 2019, ApJ, 886, 152, doi: 10.3847/1538-4357/ab4cf5

Yaron, O., & Gal-Yam, A. 2012, PASP, 124, 668, doi: 10.1086/666656

Zackay, B., Ofek, E. O., & Gal-Yam, A. 2016, ApJ, 830, 27, doi: 10.3847/0004-637X/830/1/27

Zheng, W., Kelly, P. L., & Filippenko, A. V. 2018, ApJ, 858, 104, doi: 10.3847/1538-4357/aabaeb